Molecular Mechanisms of Neurotransmitter Release Control Distinct Features of Sensory Coding Reliability

Eyal Rozenfeld[1, 2], Nadine Ehmann[3], Julia E. Manoim[1], Robert J. Kittel[3#] and Moshe Parnas[1, 2#]

1. Department of Physiology and Pharmacology, Sackler School of Medicine, Tel Aviv University, Tel Aviv 69978, Israel
2. Sagol School of Neuroscience, Tel Aviv University, Tel Aviv 69978, Israel
3. Department of Animal Physiology, Institute of Biology, Leipzig University, 04103 Leipzig, Germany

Co-Corresponding authors, email: mparnas@tauex.tau.ac.il, kittel@uni-leipzig.de

Abstract

A key requirement for the repeated identification of a stimulus is a reliable neural representation each time it is encountered. Neural coding is often considered to rely on two major coding schemes: the firing rate of action potentials, known as rate coding, and the precise timing of action potentials, known as temporal coding. Synaptic transmission is the major mechanism of information transfer between neurons. While theoretical studies have examined the effects of neurotransmitter release probability on neural code reliability, it has not yet been addressed how different components of the release machinery affect coding of physiological stimuli *in vivo*. Here, we use the first synapse of the *Drosophila* olfactory system to show that the reliability of the neural code is sensitive to perturbations of specific presynaptic proteins controlling distinct stages of neurotransmitter release. Notably, the presynaptic manipulations decreased coding reliability of postsynaptic neurons only at high odor intensity. We further show that while the reduced temporal code reliability arises from monosynaptic effects, the reduced rate code reliability arises from circuit effects, which include the recruitment of inhibitory local neurons. Finally, we find that reducing neural coding reliability decreases behavioral reliability of olfactory stimulus classification.

Keywords:

Neural code reliability, temporal code, rate code, *Drosophila*, olfaction, presynaptic function

Introduction

Animals encounter the same stimuli repeatedly and are able to recognize them over and over again. A key requirement for repeated identification of a stimulus is that its representation by the neural code will be reliably repeated on each occasion. Coding of an external stimulus by the nervous system begins at the receptor neurons. The code then undergoes transformations as it propagates to higher brain regions. Thus, reliable transmission between neurons should be required to maintain reliable neural coding.

Two major approaches are used to describe neural coding (Panzeri et al., 2010). The first is rate coding, in which the firing rate of action potentials over a period of time is employed as the neural code. The second is temporal coding, in which the precise timing and the precise pattern of action potentials is utilized for coding. Often, a combination of the two strategies is used as the coin of information for neural coding: the firing rate within a relatively small time window along with changes in firing rate over time (rather than precise action potential timing).

Chemical synaptic transmission is the major mode of fast information transfer between neurons. The response of a postsynaptic neuron depends on neurotransmitter release from synaptic vesicles (SVs) fusing with the plasma membrane of the presynaptic active zone (AZ). SV fusion, in turn, is regulated by the complex interplay of various specialized AZ proteins in a multi-step process (Südhof, 2012). Numerous theoretical studies have examined the effects of SV release probability on the reliability of the neural code. In general, it is agreed that increased release probability results in increased reliability (Kandaswamy et al., 2010; Rotman and Klyachko, 2013; Tiesinga et al., 2008; Tsodyks and Markram, 1997; Wang et al., 2010; Yang and Xu-Friedman, 2013; Yu et al., 2012; Zador, 1998). However, other models have concluded that high SV release probability is not a necessary condition in order to achieve optimal transmission of information (Arleo et al., 2010) or that reliable events are primarily elicited by synapses in a state of low

release probability (Fellous and Corral-Frías, 2015). Despite these theoretical studies, there is a lack of *in vivo* work demonstrating that changes in neurotransmitter release properties affect neural code reliability. In an elegant study in the mouse cerebellum, it was demonstrated that individual mossy fiber input pathways possess specific presynaptic functional signatures and produce distinct first spike latencies in postsynaptic granule cells. Thus, input-specific SV release properties contribute to temporal coding in this neural system (Chabrol et al., 2015). To date, however, the roles of specific presynaptic proteins in shaping neural code reliability have not yet been examined. Furthermore, mechanisms of SV release are highly dynamic and can change on the time scale of milliseconds. Among the factors that influence presynaptic function are Ca^{2+} dynamics, SV availability, and activity-dependent modulations of the release machinery (Davis and Müller, 2015; Goel and Dickman, 2021; Hallermann and Silver, 2013; Kaeser and Regehr, 2017; Kittel and Heckmann, 2016; Monday et al., 2018; Neher and Brose, 2018). In recent years, much progress has been made in identifying the role of specialized AZ proteins in the chain of events leading to SV release (Jahn and Fasshauer, 2012; Südhof, 2012; Walter et al., 2018). However, it is not known how different molecular components of the release machinery affect neural code reliability to physiological stimuli *in vivo*.

The *Drosophila* olfactory system is highly amenable to genetic manipulations and is suitable to examine how molecular mechanisms of synaptic function affect neural code reliability. In flies, odors activate olfactory receptor neurons (ORNs). Each ORN expresses a single odorant receptor gene (Buck and Axel, 1991; Hallem and Carlson, 2004; Vosshall et al., 1999). Approximately 20-40 ORNs expressing the same receptor send their axons to a single glomerulus in the antennal lobe (AL) (Gao et al., 2000; Mombaerts et al., 1996; Vosshall et al., 2000). Approximately 2-5 second-order projection neurons (PNs), in turn, send their dendrites to a single glomerulus (Tanaka et al., 2012) and each PN samples all arriving ORNs (Kazama and Wilson, 2009). The synaptic connection between an individual ORN and PN harbors ~10-30 release sites (scaling

with glomerulus size) possessing a high average release probability (~0.75) (Kazama and Wilson, 2008). The AL also contains multi-glomeruli inhibitory GABAergic and glutamatergic local neurons (iLNs) and excitatory cholinergic LNs (eLNs) (Liu and Wilson, 2013; Olsen et al., 2007; Root et al., 2008; Shang et al., 2007). The ORN-PN synapse is mainly modulated by the GABAergic iLNs (Olsen and Wilson, 2008; Root et al., 2008). Importantly, both rate coding and temporal coding were shown to be involved in insects' olfactory processing (Badel et al., 2016; Mazor and Laurent, 2005; Olsen et al., 2010; Stopfer et al., 2003). Thus, the *Drosophila* ORN-PN connection is a system with a reliable synapse, which can be genetically modified and examined in the context of physiological odor stimuli. In addition, it offers a well-defined convergence architecture with no unspecific inputs and with the option of blocking undesired circuit effects (e.g. iLNs).

Here, using *in vivo* patch-clamp recordings from over 1000 neurons, we show that knocking down SV- and AZ-associated proteins specifically in ORNs decreases the reliability of the neural code in the postsynaptic PNs to physiological odor stimuli. Our results demonstrate that interfering with SV release from ORN AZs affects the PN neural code in three ways. First, the initial transient phase of the odor response, when PNs reach their highest firing rates, becomes more variable due to reduced recruitment of iLNs. Second, the onset of the odor response is delayed and more variable. Third, the temporal dynamics of the odor response become less reliable; this third result does not involve any circuit motifs and results from monosynaptic effects. We further show that decreased expression of Ca_v2-type voltage-gated Ca^{2+} channels at ORN AZs affects neural code reliability only at high stimulus intensity. Finally, our work links reduced neural coding reliability to a reduction in the behavioral ability to correctly classify an olfactory stimulus. Taken together, the presented results suggest that the influence of ORN AZ proteins on temporal code reliability of PNs arises from monosynaptic effects at the ORN-PN synapse, whereas the influence of ORN AZ proteins on rate code reliability of PNs arises from a circuit effect, which includes the recruitment of iLNs.

Results

The molecular composition of ORN AZs affects olfactory coding reliability at high odor intensities

In order to investigate how molecular properties of the AZ influence the olfactory neural code, we used RNA interference (RNAi) to knock down key presynaptic proteins in ORNs and recorded postsynaptic PN responses to odor presentation using whole-cell current-clamp recordings. Because synaptic neurotransmitter release is a highly regulated multi-step process, we selected proteins that participate in various stages of SV recruitment to the AZ and fusion at release sites. Four proteins were targeted: I. Cacophony (Cac), the pore-forming subunit of the *Drosophila* Ca_v2-type Ca^{2+} channel, which mediates Ca^{2+}-influx at the AZ (Hallermann et al., 2010; Kawasaki et al., 2000). II. Bruchpilot (Brp), a core component of the AZ cytomatrix, which clusters Cac channels to ensure high release probability and tethers SVs to sustain transmitter release during high frequency transmission (Hallermann et al., 2010; Kittel et al., 2006). III. Synapsin (Syn), a SV-associated phospho-protein that is involved in the organization of SV pools (Gitler et al., 2004; Klagges et al., 1996; Winther et al., 2015). IV. Complexin (Cpx), an important regulator of the SNARE fusion machinery that also contributes to SV recruitment at *Drosophila* AZs (Brose, 2008; Huntwork and Littleton, 2007; Reim, 2016; Scholz et al., 2019; Trimbuch and Rosenmund, 2016).

In order to study the impact of AZ manipulations on olfactory coding, we carried out *in vivo* whole-cell current-clamp recordings. Since different odors elicit different firing rates and temporal dynamics in ORNs (Hallem et al., 2004) we tested PN responses to five different odors (Isopenthyl acetate, linalool, 2-heptanone, ethyl acetate and isobutyl acetate) and used high odor concentrations to minimize variations in ORN responses (Nagel and Wilson, 2011). To examine stimulus-evoked response reliability we recorded PN responses to 10 applications of each odor (Figure 1A and Figure S1). *Orco-GAL4* was used to drive either *UAS-Brp*^{RNAi}, *UAS-Cpx*^{RNAi}, *UAS-Cac*^{RNAi} or *UAS-Syn*^{RNAi} specifically in ORNs and *GH146-QF*, which labels approximately 60% of

PNs (Stocker et al., 1997), was used to drive *QUAS-GFP* for targeted patch-clamp recordings. We confirmed RNAi efficiency for Syn, Brp and Cpx by expressing the constructs in motoneurons and immunostaining larval neuromuscular junctions (NMJs, Figure S2). As an antibody is not available for *Drosophila* Cac, we performed *in vivo* Ca^{2+} imaging via two-photon microscopy during odor stimulation. *Orco-GAL4* was used to drive *UAS-Cac*^{RNAi} along with *UAS-GCaMP6f*. As expected, Ca^{2+} signals were significantly reduced in ORN terminals when Cac was targeted by RNAi (Figure S3A). In contrast, knockdown of Cpx (*UAS-Cpx*^{RNAi}) did not alter ORN Ca^{2+} signals, thus serving as a specificity control (Figure S3A). All genetic manipulations of presynaptic proteins significantly reduced odor-induced PN activity (Figure 1B and Figure S3B), illustrating that SV release from ORNs was decreased, though not completely abolished.

A number of different methods can be used to examine neural code reliability. Correlation-based measurement of coding reliability examines the reliability of the temporal dynamics (temporal coding) of neural activity by analyzing the activity time-series as a single entity (Schreiber et al., 2003). Thus, this analysis examines the pattern of the response over time, but does not consider the magnitude of the response. Therefore, correlation measurements do not account for variations in firing rate at a specific time point (Figure S4A, C). Another measure of temporal code reliability is the latency of the first spike following odor presentation, which was show to encode odor identify and intensity (Egea-Weiss et al., 2018). The standard deviation of response magnitude examines response reliability for a given time point or a given firing rate (rate coding) and does not account for the temporal dynamics (Figure S4B, C) (Bhandawat et al., 2007).

At high odor concentration, correlation analysis using spike trains that were integrated at increasingly wider temporal windows (Figure S4A), revealed that for wild type (*wt*) flies the response reliability (correlation value) became saturated at ~20 ms (Figure 2A, B), consistent with previous reports (Fellous and Corral-Frías, 2015; Jeanne and Wilson, 2015). Knockdown of the

presynaptic target proteins decreased overall correlation values (Figure 2A, B and Figure S5A) and increased the temporal integration window required to reach saturation (Figure 2A, B and Figure S5A, B). This demonstrates that molecular perturbations of ORN AZ function decrease the temporal reliability of PN responses. Standard deviations of PN firing rate, as a function of the mean firing rate during a 20 ms time window, also revealed a decrease in PN reliability in the RNAi lines (Figure 2C and Figure S5C) with PNs showing increased variability especially at high firing rates.

PN somata, which are accessed during patch-clamp recording, are distant from the action potential initiation site (Gouwens and Wilson, 2009; Ravenscroft et al., 2020). As a result, action potentials recorded at the soma in current-clamp mode are very small, often reaching only 5 mV in amplitude (Gouwens and Wilson, 2009). Such small action potentials are frequently not identified during the rising phase of the odor response. To better detect the first action potential, indicating the response onset, we therefore repeated this set of experiments in voltage-clamp mode. Indeed, voltage-clamp recordings enabled detection of more action potentials in the first 25 ms of the odor response and the latency of the first action potential was shorter (Figure 2D-F). As with the other reliability measurements, this analysis revealed that knocking down the presynaptic target proteins resulted in lower reliability, reflected by both increased latency and increased standard deviation of the first action potential (Figure 2G, H and Figure S6).

High odor concentrations elicit very high firing rates in ORNs that may reach up to 300 Hz (Hallem and Carlson, 2006). To examine the effect of AZ manipulations at lower ORN firing rates we selected Cac^{RNAi}, as this genotype produced a pronounced effect on PN response reliability, and repeated the above experiment using a weaker odor intensity. Interestingly, we found that under these conditions, coding reliability by PNs was not decreased by reduced Cac expression (Figure 2I-K). Taken together, our data show that different molecular components controlling presynaptic

SV release affect the reliability of the postsynaptic odor response. Furthermore, these effects are primarily evident during the presentation of a strong olfactory stimulus.

The above results suggest that high-frequency synaptic transmission is most sensitive to molecular manipulations of the ORN release machinery. High firing rates usually occur at the beginning of the odor response within the first 200 ms (Figure 1B). Thus, we examined the effects of presynaptic protein knockdown without the initial phase of the odor response. The initial phase of the odor response is characterized by a strong increase in firing rate that is highly correlated. Thus, as expected, removing the first 200 ms of the odor response from the analysis resulted in an overall decrease in correlation (Figure 3A compare to Figure 2A). Targeting presynaptic proteins via RNAi decreased the correlation further with the exception of Brp^{RNAi} (Figure 3A, B). In contrast, the increased standard deviation of PN firing rates that was observed upon reducing presynaptic target protein expression was now completely abolished. No difference in the standard deviation was observed between *wt* and RNAi flies even though high firing rates were still obtained in the sustained phase of the odor response (Figure 3C). The effect of the RNAi lines was not equally distributed throughout the initial phase of the odor response, rather presynaptic protein knockdown was most notable when the PNs reached their peak firing rate, approximately 20ms after the response onset (Figure 3D). These results suggest that two different mechanisms underlie the reduced response reliability of PNs, one affecting the reliability of the temporal code and the other affecting rate code reliability.

Knockdown of Cac reduces release probability and increases synaptic latency and jitter

Our presynaptic manipulations of ORNs significantly reduced PN spiking (Figure 1). Nevertheless, PNs maintained a substantial response to odors, demonstrating that synaptic transmission from ORNs to PNs remained principally functional in the RNAi lines. Cac is a key regulator of SV release probability at *Drosophila* neuromuscular AZs. Its functional disruption in a temperature-

sensitive mutant, RNAi-mediated knockdown, and impaired AZ channel clustering all lead to greatly decreased eEPSC (evoked excitatory postsynaptic current) amplitudes at the NMJ, especially at low stimulation frequencies (Hallermann et al., 2010; Kawasaki et al., 2000; Kittel et al., 2006). We were therefore intrigued by the observation that Cac affected PN coding reliability only at high and not at low ORN firing rates. To better understand this phenomenon, we characterized functional properties of the ORN-PN synapse in *wt* and Cac^{RNAi} animals (Figure 4A).

Surprisingly, the average eEPSC amplitude of Cac^{RNAi} flies did not differ from *wt* (Figure 4B). However, Cac knockdown led to increased paired-pulse facilitation at short interpulse intervals (Figure 4C, D), consistent with a decrease in SV release probability upon reduced expression of AZ Ca^{2+} channels. In line with a drop in release probability, Cac^{RNAi} synapses also displayed significantly elevated synaptic delay (eEPSC latency; Figure 4E), which was accompanied by an increase in the jitter of eEPSC (Figure 4F). Interestingly, both parameters progressively increased with stimulation frequency in the transgenic animals (Figure 4E, F). Within our sampling range (1, 10, 20, 60 Hz), the effect of presynaptic Cac^{RNAi} on these temporal parameters was most pronounced at 60 Hz.

Taken together, these results suggest a homeostatic mechanism at the ORN-PN synaptic connection, which compensates the drop in release probability caused by presynaptic Cac knockdown to maintain normal eEPSC amplitudes. However, this compensation does not cover the temporal properties of synaptic transmission. The reduced release probability of Cac^{RNAi} ORNs generates longer synaptic latencies with larger eEPSC jitter, consistent with increased first spike latencies and jitter during odor application. Thus, while the ORN-PN synapse is surprisingly resilient to Ca^{2+} channel perturbations, Cac knockdown delays synaptic transmission and reduces the temporal precision of synaptic signaling.

Monosynaptic effects and circuit activity underlie distinct features of coding reliability

Next, we turned to examine whether the diminished coding reliability caused by *Cac*^{RNAi} is due to monosynaptic mechanisms or instead arises from circuit effects. GABAergic iLNs also receive their major input from ORNs and inhibit these presynaptically. Whereas PNs are uniglomerular and receive homogenous ORN input, iLNs are multiglomerular and receive heterogeneous ORN input. PNs respond to ORN activity in a non-linear manner (Bhandawat et al., 2007; Kazama and Wilson, 2008; Olsen et al., 2010). In contrast, GABAergic iLNs respond linearly to ORN activity (Olsen et al., 2010), are more sensitive to reduced input from ORNs (Rozenfeld et al., 2019), and show a stronger transiency in their odor response (Nagel et al., 2015). Thus, we speculated that at least some of the observed reduction in PN reliability following presynaptic manipulations might arise from reduced recruitment of iLNs. In particular, this may explain the increased standard deviation in the RNAi lines that no longer occurred in the absence of the initial transient phase of PN odor responses (Figure 3C, D). To examine how iLN activity affects PN odor response reliability we compared *wt* and presynaptic *Cac*^{RNAi} flies. *Orco-GAL4* again drove *UAS-Cac*^{RNAi} and *449-QF* was used to express *QUAS-GFP* in iLNs (Chen et al., 2019). Reducing Cac protein levels in ORNs resulted in an almost complete abolishment of iLN responses to odors (Figure 5A, B). We then examined the effects of blocking GABAergic transmission on PN reliability. To this end, we exposed the brain to 100 µM CGP54626, a selective $GABA_B$ receptor antagonist, and 250 µM picrotoxin, a chloride channel blocker (Etter et al., 2002) and antagonist of $GABA_A$ receptors (Figure 5C). As expected, GABA blockers affected *wt* firing rates (Figure 5D) but had no effect on PN spiking in *Cac*^{RNAi} flies, where iLNs are hardly recruited (Figure 5B). When blocking GABA receptors in *wt* flies, we observed a significant increase in the variability of PN activity but the temporal integration window of PN responses was unaffected (Figure 5E). This suggests that iLNs affect rate code but not temporal code reliability. Since the odor response of iLNs was diminished when Cac was knocked down in ORNs we expected that blocking GABA

receptors would not further affect coding reliability in *Cac*^{RNAi} flies. Indeed, blocking GABAergic transmission had no effect whatsoever on variability and only a minor effect on the temporal integration window in presynaptic *Cac*^{RNAi} (Figure 5E). Together, these experiments suggest that iLNs affect rate code but not temporal code reliability.

The AL also contains another population of inhibitory local neurons, which release glutamate. These glutamatergic interneurons mainly inhibit PNs, but were shown to have effectively similar roles as the GABAergic iLNs on the activity of the AL neural circuit (Liu and Wilson, 2013). Thus, the pharmacological experiments affect both the presynapse of ORNs and the postsynapse of PNs. Since iLNs mainly act by activating GABA-B receptors in the presynaptic terminal of ORNs (Olsen and Wilson, 2008; Root et al., 2008), we tested whether driving *GABA-B-R2*^{RNAi} (Perkins et al., 2015) in ORNs has similar effects on PN coding reliability as pharmacologically blocking the inhibitory iLNs (Figure 5F). Indeed, *GABA-B-R2*^{RNAi} decreased rate code reliability at high firing rates but did not affect the temporal integration window (Figure 5G). The glutamatergic iLNs inhibit PNs by activating the glutamate receptor GluClα (Figure 5H). Therefore, we expressed an RNAi construct against GluClα in PNs and tested their odor response and coding reliability. Knockdown of the GluClα receptor in PNs had a strong effect on coding variability, as observed for the pharmacological experiments and by blocking the inhibitory presynaptic circuit (Figure 5I). In addition, we also observed an overall decrease in correlation (Figure 5I). However, in contrast to all AZ perturbations which increased PN integration time (Figure 2B), we did not observe any such increase in GluClα^{RNAi}, if at all, the integration time of PNs was slightly decreased (Figure 5I and Figure S7).

In summary, both pharmacological and genetic approaches suggest that the inhibitory AL circuit affects PNs rate code variability but not temporal reliability. Together with the increased latency and jitter of the ORN-PN synapse, these results indicate that our molecular manipulations of ORN

AZ function change the temporal code reliability of PNs monosynaptically, whereas the rate code reliability of PNs is altered via a circuit effect that includes the recruitment of iLNs.

Reducing neural coding reliability disrupts behavioral reliability

The above results demonstrate that knocking down specific presynaptic proteins decreases neural coding reliability. To examine whether these changes are strong enough to affect behavioral output we tested the flies' ability to correctly classify an ecologically relevant stimulus. To reduce response variability, which is often observed for naïve behavior (Lerner et al., 2020; Parnas et al., 2013), we paired isopentyl acetate with an electric shock, using a well-established custom built apparatus (Bielopolski et al., 2019; Claridge-Chang et al., 2009; Lerner et al., 2020; Parnas et al., 2013; Rozenfeld et al., 2019) and tested the accuracy of the animals' behavioral responses, i.e. avoidance of isopentyl acetate. Following prolonged exposure (2 minutes) to the olfactory stimulus, presynaptic Cac^{RNAi} animals were equally successful as their parental controls in classifying the odor (Figure 6A, B). However, when flies navigate in their natural habitat, olfactory stimuli are often brief and repetitive. Since such short stimuli could not be delivered in the above paradigm, we used an alternative assay in which the flies walked on a Styrofoam ball. This setting allowed us to present the same pattern of olfactory stimuli as used for the electrophysiological recordings (Figure 2). Ten one-second trials of the shock-paired odor isopentyl acetate were presented and the behavioral response was classified as correct if flies turned away from the odor source (Figure 6C). Indeed, Cac^{RNAi} flies made significantly fewer correct choices as a result of identifying isopentyl acetate less reliably (Figure 6D). This reduction in correct stimulus classification was not due to a learning defect since the learning index was similar between *wt* and Cac^{RNAi} flies (Figure 6B). Furthermore, Cac knockdown was only performed in the first order ORNs and not in third order neurons, which are required for memory formation (Modi et al., 2020). Thus, the molecular integrity of ORN AZs affects both the coding reliability of PNs and the animal's ability to classify an important physiological stimulus.

Discussion

Using *in vivo* recordings, we show that the molecular integrity of ORN AZs is required for a reliable neural code in the postsynaptic PNs in response to physiological odor stimuli. Knockdown of presynaptic proteins involved in specific stages of neurotransmitter release from AZs affected neural code reliability in three manners. First, the high firing rates of the initial transient phase of PN odor responses became more variable due to reduced recruitment of iLNs. Second, the onset of odor responses was delayed and more variable. Third, the temporal dynamics of the odor response became less reliable. This third effect results most probably from monosynaptic changes to ORN-PN transmission. At a behavioral level, we find that reduced coding reliability of PNs impairs the animals' ability to correctly classify a physiologically relevant stimulus. In summary, these findings support a model where the reliability of temporal coding by PNs depends on monosynaptic transmission from ORNs whereas the reliability of rate coding by PNs depends on circuit effects that include the recruitment of iLNs.

We found that knocking down AZ proteins affected neuronal coding reliability mainly at high firing rates. This was true for both the monosynaptic as well as the circuit mechanisms. In terms of the circuit effects on rate code reliability, this is in line with the recruitment of iLNs. iLNs sample many types of ORNs with different response profiles (Hallem and Carlson, 2006) and as a result, they respond linearly to ORN activity (Olsen et al., 2010). Thus, iLNs respond most strongly to high ORN firing rates, which in turn are triggered by high odor intensities. Correspondingly, almost entirely eliminating the recruitment of iLNs by manipulating ORN AZs (Figure 5), mostly affects processing of high firing rates. For the monosynaptic mechanisms, which control temporal code reliability, we focused on Cac^{RNAi} as a case study. Here, we find that a decrease in SV release probability increases the latency and jitter of eEPSC (Figure 4), accompanied by an increase in the latency and jitter of postsynaptic action potential initiation (Figure 2). We further show that this

drop in the temporal precision of synaptic transmission increases in a frequency-dependent manner. This finding helps to explain why disrupted AZ function mainly impairs temporal coding at high firing rates and strong odor intensities.

Theoretical studies have suggested that decreasing SV release probability should result in reduced neural coding reliability (Kandaswamy et al., 2010; Rotman and Klyachko, 2013; Tiesinga et al., 2008; Tsodyks and Markram, 1997; Wang et al., 2010; Yang and Xu-Friedman, 2013; Yu et al., 2012; Zador, 1998), although exceptions have also been demonstrated (Arleo et al., 2010; Fellous and Corral-Frías, 2015). However, whether these theoretical studies hold true *in vivo*, with highly dynamic synaptic properties, in complex neural circuits, and in response to physiological stimuli has remained an open question. To the best of our knowledge, the present study provides the first *in vivo* evidence that interfering with the molecular control of SV release results in reduced neural coding reliability. Notably, the ORN-PN synapse is surprisingly resilient to reduced AZ Ca^{2+} channel expression and appears to be able to compensate the drop in release probability by increasing the number of release sites and/or by elevating postsynaptic sensitivity to yield normal eEPSC amplitudes. Homeostatic synaptic plasticity features at the *Drosophila* NMJ (Davis and Müller, 2015; Goel and Dickman, 2021), mushroom body (Apostolopoulou and Lin, 2020), and also operates in the antennal lobe to match synaptic strength to PN excitability (Harrell et al., 2021; Kazama and Wilson, 2008). Interestingly, Cac^{RNAi} decreases synaptic transmission to a greater extent from ORNs to iLNs than from ORNs to PNs (compare Figures 1B and 5B). Thus, the functional impact of Cac or mechanisms to compensate for reduced Ca^{2+} channel expression may differ between ORN AZs depending on the identity of the postsynaptic partner. Here parallels may exist with the NMJ, where the expression of presynaptic homeostatic plasticity is compartmentalized to a subset of a motoneuron's synapses depending on their target muscle (Li et al., 2018). These considerations emphasize the importance of further future studies on the molecular heterogeneity of AZs in the olfactory system (Ehmann et al., 2018; Fulterer et al., 2018;

Pooryasin et al., 2021) and of elucidating the physiological properties of individual synapses in the context of neural information processing.

Methods

Fly Strains

Fly strains (see below) were raised on cornmeal agar under a 12 h light/12 h dark cycle at 25 ˚C. The following fly strains were used: *UAS-Cpx*^{RNAi} (BDSC_42017), *UAS-Cac*^{RNAi} (Dietzl et al., 2007) (VDRC ID 5551), *UAS-Brp*^{RNAi} (BDSC_80449), *UAS-Syn*^{RNAi} (BDSC_82983), UAS-GluClα^{RNAi} (53356), UAS-GABA-B-R2^{RNAi} (50608), *GH146-QF,QUAS-mCD8-GFP* (BDSC_30038), *Orco-GAL4* (BDSC_26818), *UAS- GCaMP6f* (BDSC_52869), *449-QF* (Chen et al., 2019), *ok6-Gal4* (Sanyal, 2009).

Olfactory stimulation

Odors (purest level available) were obtained from Sigma-Aldrich (Rehovot, Israel). Odor flow of 0.4 l/min (10^{-1} dilution) was combined with a carrier air stream of 0.4 l/min using mass-flow controllers (Sensirion) and software controlled solenoid valves (The Lee Company). This resulted in a final odor dilution of $5X10^{-2}$ delivered to the fly. Odor flow was delivered through a 1/16 inch ultra-chemical-resistant Versilon PVC tubing (Saint-Gobain, NJ, USA) placed 5 mm from the fly's antenna.

Electrophysiology

Flies were anesthetized for 1 minute on ice. A single fly was fixed to aluminum foil using wax. To expose the brain, the cuticle and trachea were removed. The brain was superfused with carbonated solution (95% O_2, 5% CO_2) containing 103 mM NaCl, 3 mM KCl, 5 mM trehalose, 10 mM glucose, 26 mM $NaHCO_3$, 1 mM NaH_2PO_4, 1.5 mM $CaCl_2$, 4 mM $MgCl_2$, 5 mM N-Tris (TES), pH 7.3. For *in vivo* whole-cell recordings 2-4 days old flies were used as previously described (Wilson and Laurent, 2005) . Briefly, flies' brains were visualized on a Scientifica SliceScope Pro 1000 upright microscope with a 40x water immersion objective. Patch pipettes of 9–12 MΩ

resistance were used. Intracellular solution contained: potassium aspartate 140mM, HEPES 10mM, KCL 1mM, MgATP 4mM, Na3GTP 0.5mM, EGTA 1mM with pH of 7.3 and osmolarity of 265 mOsm. PNs were randomly patched from both the lateral and medial cluster and iLNs were randomly patched from the lateral cluster. Voltage or current recordings were performed using Axon Instruments MultiClamp 700B amplifier in current- or voltage-clamp mode respectively. Data was low-pass filtered at 1 kHz and sampled at 50 kHz. Upon break-in to the cell, a small constant current was applied to maintain a membrane potential of -60mV. Action potential times were extracted using a custom MATLAB code followed by manual inspection to verify correct identification. Spike times were aligned to the beginning of the rising phase of the membrane potential, indicating the beginning of the odor stimulus. In experiments where GABA blockers were used, 100 µM of CGP 54626 (Tocris, CAS: 149184-21-4) and 250 µM of picrotoxin (Sigma-Aldrich, CAS: 124-87-8) were bath applied. eEPSCs were evoked by stimulating ORN axons with a minimal stimulation protocol via a suction electrode (Kazama and Wilson, 2008). Brief (typically 50µs) pulses were passed through the innervating nerve using a constant current stimulator (Digitimer, DS3 Isolated Current Stimulator). To measure eEPSC amplitude and kinetics 32 eEPSCs were evoked at 1 Hz and averaged. eEPSC latency was measured from the beginning of the stimulation artifact to the beginning of the eEPSC rising phase. Paired-pulse recordings were made at 0.2 Hz with inter-stimulus intervals of (in ms): 10, 30, 100, 300 and 1,000. For each interval 20 traces were averaged. Ten seconds of rest were afforded to the cell in between recordings. The amplitude of the second response in 10 ms inter-pulse recordings was measured from the peak to the point of interception with the extrapolated first response. Data were analyzed using MATLAB.

Functional Imaging

Flies used for functional imaging were reared as described above. Imaging was done as previously described (Bielopolski et al., 2019; Israel et al., 2020; Lerner et al., 2020). Briefly, using

two-photon laser-scanning microscopy (DF-Scope installed on an Olympus BX51WI microscope). Flies were anesthetized on ice then a single fly was moved to a custom built chamber and fixed to aluminum foil using wax. Cuticle and trachea in the required area were removed, and the exposed brain was superfused with carbonated solution as described above. Odors at final dilution of $5X10^{-2}$ were delivered as described above. Fluorescence was excited by a Ti-Sapphire laser (Mai Tai HP DS, 100 fs pulses) centered at 910 nm, attenuated by a Pockels cell (Conoptics) and coupled to a galvo-resonant scanner. Excitation light was focused by a 20X, 1.0 NA objective (Olympus XLUMPLFLN20XW), and emitted photons were detected by GaAsP photomultiplier tubes (Hamamatsu Photonics, H10770PA-40SEL), whose currents were amplified (Hamamatsu HC-130-INV) and transferred to the imaging computer (MScan 2.3.01). All imaging experiments were acquired at 30 Hz.

Immunohistochemistry

Staining of *Drosophila* larval NMJs followed a standard protocol (Ljaschenko et al., 2013). In brief, third instar larvae were dissected in Ca^{2+}-free HL-3 [Haemolymph-like solution; (Stewart et al., 1994)], fixed in 4% paraformaldehyde for 10 min at room temperature and blocked with PBT (0.05% Triton X-100; T8787, Sigma Aldrich) supplemented with 5% normal goat serum (G9023, Sigma Aldrich) for 30 min. Antibodies were used in the following dilutions (in blocking solution): mouse-α-Brp (nc82; 1:100; provided by E. Buchner; RRID:AB_2314866), rabbit-α-Cpx (1:500;Huntwork and Littleton, 2007; RRID: AB_2568068), mouse-α-Syn (1:30, Developmental Studies Hybridoma Bank; RRID:AB_528479), goat-α-Hrp conjugated with Alexa Fluor 488 (1:250; Jackson ImmunoResearch; RRID: AB_2338965), goat-α-mouse STAR RED (1:200; Abberior; RRID:AB_2810982), goat-α-rabbit STAR RED (1:200; Abberior RRID:AB_2833015). Primary antibodies were incubated at 4°C overnight. This was followed by 2 short and 3 x 20 min washing steps with PBT and incubation with secondary antibodies for 2 h at room temperature. Subsequently, samples were washed (2 short, 3 x 20 min washing steps) before mounting in

Vectashield (H-1000, Vector laboratories). Images were acquired with a Zeiss Imager.Z2 confocal system (objective: 63 x, numerical aperture 1.4, oil). Control animals and individual RNAi lines were stained in the same vial and imaged with identical laser settings before laser power was increased. For staining, flies were kept at 29 degrees.

Behavioral chambers

Experiments were performed using a custom-built, fully automated apparatus (Bielopolski et al., 2019; Claridge-Chang et al., 2009; Parnas et al., 2013). Single flies were housed in clear chambers (polycarbonate, length 50 mm, width 5 mm, height 1.3 mm). Mass flow controllers (CMOSens PerformanceLine, Sensirion) were used to control air flow. An odor stream (0.3 l/min) obtained by circulating the air flow through vials filled with a liquid odorant was combined with a carrier flow (2.7 l/min). Isopentyl acetate was prepared at 10 fold dilution in mineral oil. Liquid dilution and mixing carrier and odor stimulus stream resulted in a final 100 fold dilution. Fresh odors were prepared daily.

Two identical odor delivery systems were used each delivering odors independently to each half of the chamber. The total flow (3 l/minute, carrier and odor stimulus) was split between 20 chambers. . The air flow from the two halves of the chamber converged at a central choice zone. The 20 chambers were stacked in two columns each containing 10 chambers and were backlit by 940 nm LEDs (Vishay TSAL6400). Images were obtained by a MAKO CMOS camera (Allied Vision Technologies) equipped with a Computar M0814-MP2 lens. The apparatus was operated in a temperature controlled incubator (Panasonic MIR 154) at 25℃.

Fly position was extracted from video images using a virtual instrument written in LabVIEW 7.1 (National Instruments). The same virtual instrument was also used to control odor delivery. Data were analyzed in MATLAB 2018a (The MathWorks). Conditioning protocol included 12 equally spaced 1.25 s electric shocks at 50 V, and was repeated twice. The learning index was calculated

as (preference for isopentyl acetate before training) – (preference for isopentyl acetate after training). Flies that were used for the ball assay in figure 4C were given a training protocol that consisted of 12 equally spaced 1.25 s electric shocks at 50 V, and repeated 6 times with 15 minutes interval. Flies were then tested on the ball assay 12 hours later.

Ball assay

Flies walked on a treadmill ball as previously described (Seelig et al., 2010). Briefly, the fly thorax was glued to a fine metal rod using wax in a manner that allowed for free limb movement. Flies were then placed on a Styrofoam ball with a diameter of 9 mm which floated on an air-steam in a custom made ball holder. Videos were captured using a Blackfly S (FLIR® Systems) camera fitted with a Computar Macro zoom 0.3–1×, 1:4.5 lens at a frame rate of 100 FPS. The ball was illuminated by infrared LEDs and the fly position was tracked offline using FicTrac (Moore et al., 2014). Odor delivery was the same as for the electrophysiological recording experiments described above.

Quantification and statistical analysis

Integration window analysis

For this analysis, only the first two seconds after the beginning of the odor stimulus were used. Spike trains were then binned with bin sizes ranging from 1ms to 200ms with 1ms intervals. For each bin size, the pairwise Pearson correlation was calculated for all combinations of the 10 trials for each odor. Trials that did not show any odor response were excluded from this analysis. Integration window was defined as the Youden's index (Youden, 1950), which is the point of maximal distance between the correlation vs. bin size curve and the diagonal between the minimum and maximum point of said curve.

Variance analysis

For each fly, the mean and variance of the 10 stimuli repetitions were calculated using time bins of 20ms. The mean spike count of each bin was then binned into discrete bins along with the corresponding variance in that time bin.

Statistics and data analysis

All statistical testing and parameter extraction were done using custom MATLAB code (The MathWorks, Inc.). All statistical tests details can be found in table S1. Significance was defined as a p-value smaller than 0.05 and all statistical tests were two-sided.

Effect size was calculated with the Measures of Effect Size (MES) Toolbox https://github.com/hhentschke/measures-of-effect-size-toolbox/blob/master/readme.md).

For presentation, bar plots with dots were generated using the UnivarScatter MATLAB ToolBox (https://www.mathworks.com/matlabcentral/fileexchange/54243-univarscatter), raster plots were generated with the Flexible and Fast Spike Raster Plotting ToolBox (https://www.mathworks.com/matlabcentral/fileexchange/45671-flexible-and-fast-spike-raster-plotting) and the shadedErrorBar function (https://github.com/raacampbell/shadedErrorBar) for shaded errors on imaging traces.

Data and code availability

Examples of the data and code used to generate the figures in this manuscript are available upon publication in the first author GitHub page: https://github.com/Eyal-ro.

Acknowledgments

We thank Dr. Ya-Hui Chou and the Bloomington Stock Center for fly strains. This work was supported by the European Research Council (676844, MP) and the Deutsche

Forschungsgemeinschaft (project numbers 430156010/SPP 2205 to RJK and 408264519 to MP and RJK).

Author contributions

ER: conceptualization, methodology, investigation, formal analysis, software, writing–review & editing, visualization. NE: investigation, formal analysis, writing–review & editing, visualization JEM: investigation, formal analysis, visualization. RJK: Initiated the project, conceptualization, methodology, writing–original draft, writing–review & editing, supervision, funding acquisition. MP: Initiated the project, conceptualization, methodology, investigation, formal analysis, software, writing–original draft, writing–review & editing, visualization, supervision, funding acquisition.

References

Apostolopoulou AA, Lin AC. 2020. Mechanisms underlying homeostatic plasticity in the Drosophila mushroom body in vivo. *Proc Natl Acad Sci U S A* **117**:16606–16615. doi:10.1073/PNAS.1921294117/-/DCSUPPLEMENTAL

Arleo A, Nieus T, Bezzi M, D'Errico A, D'Angelo E, Coenen OJMD. 2010. How synaptic release probability shapes neuronal transmission: Information-theoretic analysis in a cerebellar granule cell. *Neural Comput*. doi:10.1162/NECO_a_00006-Arleo

Badel L, Ohta K, Tsuchimoto Y, Kazama H. 2016. Decoding of Context-Dependent Olfactory Behavior in Drosophila. *Neuron* **91**:155–167. doi:10.1016/J.NEURON.2016.05.022

Bhandawat V, Olsen SR, Gouwens NW, Schlief ML, Wilson RI. 2007. Sensory processing in the Drosophila antennal lobe increases reliability and separability of ensemble odor representations. *Nat Neurosci* **10**:1474–1482. doi:10.1038/nn1976

Bielopolski N, Amin H, Apostolopoulou AA, Rozenfeld E, Lerner H, Huetteroth W, Lin AC, Parnas M. 2019. Inhibitory muscarinic acetylcholine receptors enhance aversive olfactory learning in adult Drosophila. *Elife* **8**. doi:10.7554/eLife.48264

Brose N. 2008. For Better or for Worse: Complexins Regulate SNARE Function and Vesicle Fusion. *Traffic* **9**:1403–1413. doi:10.1111/j.1600-0854.2008.00758.x

Buck L, Axel R. 1991. A novel multigene family may encode odorant receptors: A molecular basis for odor recognition. *Cell* **65**:175–187. doi:10.1016/0092-8674(91)90418-X

Chabrol FP, Arenz A, Wiechert MT, Margrie TW, Digregorio DA. 2015. Synaptic diversity enables temporal coding of coincident multisensory inputs in single neurons. *Nat Neurosci* **18**:718–727. doi:10.1038/nn.3974

Chen YJ, Chang HH, Lin SH, Lin TY, Wu TH, Lin HJ, Liou NF, Yang CJ, Chen YT, Chang KH,

Li CY, Chou YH. 2019. Differential efficacy of genetically swapping GAL4. *J Neurogenet*. doi:10.1080/01677063.2018.1564289

Claridge-Chang A, Roorda RD, Vrontou E, Sjulson L, Li H, Hirsh J, Miesenböck G. 2009. Writing Memories with Light-Addressable Reinforcement Circuitry. *Cell* **139**:405–415. doi:10.1016/J.CELL.2009.08.034

Davis GW, Müller M. 2015. Homeostatic control of presynaptic neurotransmitter release. *Annu Rev Physiol* **77**:251–270. doi:10.1146/ANNUREV-PHYSIOL-021014-071740

Dietzl G, Chen D, Schnorrer F, Su KC, Barinova Y, Fellner M, Gasser B, Kinsey K, Oppel S, Scheiblauer S, Couto A, Marra V, Keleman K, Dickson BJ. 2007. A genome-wide transgenic RNAi library for conditional gene inactivation in Drosophila. *Nature* **448**:151–156. doi:10.1038/nature05954

Egea-Weiss A, Renner A, Kleineidam CJ, Szyszka P. 2018. High Precision of Spike Timing across Olfactory Receptor Neurons Allows Rapid Odor Coding in Drosophila. *iScience* **4**:76–83. doi:10.1016/J.ISCI.2018.05.009

Ehmann N, Owald D, Kittel RJ. 2018. Drosophila active zones: From molecules to behaviour. *Neurosci Res*. doi:10.1016/j.neures.2017.11.015

Etter A, Cully DF, Liu KK, Reiss B, Vassilatis DK, Schaeffer JM, Arena JP. 2002. Picrotoxin Blockade of Invertebrate Glutamate-Gated Chloride Channels: Subunit Dependence and Evidence for Binding Within the Pore. *J Neurochem* **72**:318–326. doi:10.1111/JNC.1999.72.1.318

Fellous J-M, Corral-Frías NS. 2015. Reliability and Precision Are Optimal for Non-Uniform Distributions of Presynaptic Release Probability. *J Biomed Sci Eng* **8**:170–183. doi:10.4236/jbise.2015.83017

Fulterer A, Andlauer TFM, Ender A, Maglione M, Eyring K, Woitkuhn J, Lehmann M, Matkovic-Rachid T, Geiger JRP, Walter AM, Nagel KI, Sigrist SJ. 2018. Active Zone Scaffold Protein Ratios Tune Functional Diversity across Brain Synapses. *Cell Rep* **23**:1259–1274. doi:10.1016/j.celrep.2018.03.126

Gao Q, Yuan B, Chess A. 2000. Convergent projections of Drosophila olfactory neurons to specific glomeruli in the antennal lobe. *Nat Neurosci* **3**:780–785. doi:10.1038/77680

Gitler D, Takagishi Y, Feng J, Ren Y, Rodriguiz RM, Wetsel WC, Greengard P, Augustine GJ. 2004. Different presynaptic roles of synapsins at excitatory and inhibitory synapses. *J Neurosci* **24**:11368–11380. doi:10.1523/JNEUROSCI.3795-04.2004

Goel P, Dickman D. 2021. Synaptic homeostats: latent plasticity revealed at the Drosophila neuromuscular junction. *Cell Mol Life Sci*. doi:10.1007/s00018-020-03732-3

Gouwens NW, Wilson RI. 2009. Signal propagation in Drosophila central neurons. *J Neurosci* **29**:6239–6249. doi:10.1523/JNEUROSCI.0764-09.2009

Hallem EA, Carlson JR. 2006. Coding of Odors by a Receptor Repertoire. *Cell* **125**:143–160. doi:10.1016/j.cell.2006.01.050

Hallem EA, Carlson JR. 2004. The odor coding system of Drosophila. *Trends Genet* **20**:453–459. doi:10.1016/J.TIG.2004.06.015

Hallem EA, Ho MG, Carlson JR. 2004. The molecular basis of odor coding in the Drosophila antenna. *Cell* **117**:965–979. doi:10.1016/j.cell.2004.05.012

Hallermann S, Kittel RJ, Wichmann C, Weyhersmüller A, Fouquet W, Mertel S, Owald D, Eimer S, Depner H, Schwärzel M, Sigrist SJ, Heckmann M, Weyhersmuller A, Fouquet W, Mertel S, Owald D, Eimer S, Depner H, Schwarzel M, Sigrist SJ, Heckmann M. 2010. Naked dense bodies provoke depression. *J Neurosci* **30**:14340–14345.

doi:10.1523/JNEUROSCI.2495-10.2010

Hallermann S, Silver RA. 2013. Sustaining rapid vesicular release at active zones: Potential roles for vesicle tethering. *Trends Neurosci*. doi:10.1016/j.tins.2012.10.001

Harrell ER, Pimentel D, Miesenböck G. 2021. Changes in Presynaptic Gene Expression during Homeostatic Compensation at a Central Synapse. *J Neurosci* **41**:3054–3067. doi:10.1523/JNEUROSCI.2979-20.2021

Huntwork S, Littleton JT. 2007. A complexin fusion clamp regulates spontaneous neurotransmitter release and synaptic growth. *Nat Neurosci* **10**:1235–1237. doi:10.1038/nn1980

Israel S, Rozenfeld E, Weber D, Huetteroth W, Parnas M. 2020. Two Parallel Pathways Mediate Olfactory-Driven Backward Locomotion. *bioRxiv*. doi:10.1101/2020.11.23.393819

Jahn R, Fasshauer D. 2012. Molecular machines governing exocytosis of synaptic vesicles. *Nature*. doi:10.1038/nature11320

Jeanne JM, Wilson RI. 2015. Convergence, Divergence, and Reconvergence in a Feedforward Network Improves Neural Speed and Accuracy. *Neuron* **88**:1014–1026. doi:10.1016/j.neuron.2015.10.018

Kaeser PS, Regehr WG. 2017. The readily releasable pool of synaptic vesicles. *Curr Opin Neurobiol*. doi:10.1016/j.conb.2016.12.012

Kandaswamy U, Deng PY, Stevens CF, Klyachko VA. 2010. The role of presynaptic dynamics in processing of natural spike trains in hippocampal synapses. *J Neurosci* **30**:15904–15914. doi:10.1523/JNEUROSCI.4050-10.2010

Kawasaki F, Felling R, Ordway RW. 2000. A Temperature-Sensitive Paralytic Mutant Defines a Primary Synaptic Calcium Channel in Drosophila.

Kazama H, Wilson RI. 2009. Origins of correlated activity in an olfactory circuit. *Nat Neurosci* **12**:1136–1144. doi:10.1038/nn.2376

Kazama H, Wilson RI. 2008. Homeostatic Matching and Nonlinear Amplification at Identified Central Synapses. *Neuron* **58**:401–413. doi:10.1016/j.neuron.2008.02.030

Kittel RJ, Heckmann M. 2016. Synaptic vesicle proteins and active zone plasticity. *Front Synaptic Neurosci* **8**. doi:10.3389/fnsyn.2016.00008

Kittel RJ, Wichmann C, Rasse TM, Fouquet W, Schmidt M, Schmid A, Wagh DA, Pawlu C, Kellner RR, Willig KI, Hell SW, Buchner E, Heckmann M, Sigrist SJ. 2006. Bruchpilot promotes active zone assembly, Ca2+ channel clustering, and vesicle release. *Science (80-)* **312**:1051–1054. doi:10.1126/science.1126308

Klagges BRE, Heimbeck G, Godenschwege TA, Hofbauer A, Pflugfelder GO, Reifegerste R, Reisch D, Schaupp M, Buchner S, Buchner E. 1996. Invertebrate synapsins: A single gene codes for several isoforms in Drosophila. *J Neurosci* **16**:3154–3165. doi:10.1523/jneurosci.16-10-03154.1996

Lerner H, Rozenfeld E, Rozenman B, Huetteroth W, Parnas M. 2020. Differential Role for a Defined Lateral Horn Neuron Subset in Naïve Odor Valence in Drosophila. *Sci Rep*. doi:10.1038/s41598-020-63169-3

Li X, Goel P, Chen C, Angajala V, Chen X, Dickman DK. 2018. Synapse-specific and compartmentalized expression of presynaptic homeostatic potentiation. *Elife* **7**. doi:10.7554/ELIFE.34338

Liu WW, Wilson RI. 2013. Glutamate is an inhibitory neurotransmitter in the Drosophila olfactory system. *Proc Natl Acad Sci U S A* **110**:10294–10299. doi:10.1073/pnas.1220560110

Ljaschenko D, Ehmann N, Kittel RJ. 2013. Hebbian plasticity guides maturation of glutamate

receptor fields in vivo. *Cell Rep* **3**:1407–13. doi:10.1016/j.celrep.2013.04.003

Mazor O, Laurent G. 2005. Transient dynamics versus fixed points in odor representations by locust antennal lobe projection neurons. *Neuron* **48**:661–673. doi:10.1016/j.neuron.2005.09.032

Modi MN, Shuai Y, Turner GC. 2020. The Drosophila Mushroom Body: From Architecture to Algorithm in a Learning Circuit. *Annu Rev Neurosci* **43**:465–484. doi:10.1146/ANNUREV-NEURO-080317-0621333

Mombaerts P, Wang F, Dulac C, Chao SK, Nemes A, Mendelsohn M, Edmondson J, Axel R. 1996. Visualizing an olfactory sensory map. *Cell* **87**:675–686. doi:10.1016/S0092-8674(00)81387-2

Monday HR, Younts TJ, Castillo PE. 2018. Long-Term Plasticity of Neurotransmitter Release: Emerging Mechanisms and Contributions to Brain Function and Disease. *https://doi.org/101146/annurev-neuro-080317-062155* **41**:299–322. doi:10.1146/ANNUREV-NEURO-080317-062155

Moore RJD, Taylor GJ, Paulk AC, Pearson T, van Swinderen B, Srinivasan M V. 2014. FicTrac: A visual method for tracking spherical motion and generating fictive animal paths. *J Neurosci Methods*. doi:10.1016/j.jneumeth.2014.01.010

Nagel KI, Hong EJ, Wilson RI. 2015. Synaptic and circuit mechanisms promoting broadband transmission of olfactory stimulus dynamics. *Nat Neurosci* **18**:56–65. doi:10.1038/nn.3895

Nagel KI, Wilson RI. 2011. Biophysical mechanisms underlying olfactory receptor neuron dynamics. *Nat Neurosci* **14**:208–216. doi:10.1038/nn.2725

Neher E, Brose N. 2018. Dynamically Primed Synaptic Vesicle States: Key to Understand Synaptic Short-Term Plasticity. *Neuron*. doi:10.1016/j.neuron.2018.11.024

Olsen SR, Bhandawat V, Wilson RI. 2010. Divisive normalization in olfactory population codes. *Neuron* **66**:287–299. doi:10.1016/j.neuron.2010.04.009

Olsen SR, Bhandawat V, Wilson RI. 2007. Excitatory interactions between olfactory processing channels in the Drosophila antennal lobe. *Neuron* **54**:89–103. doi:10.1016/j.neuron.2007.03.010

Olsen SR, Wilson RI. 2008. Lateral presynaptic inhibition mediates gain control in an olfactory circuit. *Nature* **452**:956–960. doi:10.1038/nature06864

Panzeri S, Brunel N, Logothetis NK, Kayser C. 2010. Sensory neural codes using multiplexed temporal scales. *Trends Neurosci* **33**:111–120. doi:10.1016/j.tins.2009.12.001

Parnas M, Lin AC, Huetteroth W, Miesenböck G. 2013. Odor Discrimination in Drosophila: From Neural Population Codes to Behavior. *Neuron* **79**:932–944. doi:10.1016/J.NEURON.2013.08.006

Perkins LA, Holderbaum L, Tao R, Hu Y, Sopko R, McCall K, Yang-Zhou D, Flockhart I, Binari R, Shim HS, Miller A, Housden A, Foos M, Randkelv S, Kelley C, Namgyal P, Villalta C, Liu LP, Jiang X, Huan-Huan Q, Wang X, Fujiyama A, Toyoda A, Ayers K, Blum A, Czech B, Neumuller R, Yan D, Cavallaro A, Hibbard K, Hall D, Cooley L, Hannon GJ, Lehmann R, Parks A, Mohr SE, Ueda R, Kondo S, Ni JQ, Perrimon N. 2015. The transgenic RNAi project at Harvard medical school: Resources and validation. *Genetics* **201**:843–852. doi:10.1534/GENETICS.115.180208/-/DC1

Pooryasin A, Maglione M, Schubert M, Matkovic-Rachid T, Hasheminasab S mohammad, Pech U, Fiala A, Mielke T, Sigrist SJ. 2021. Unc13A and Unc13B contribute to the decoding of distinct sensory information in Drosophila. *Nat Commun* **12**:1–14. doi:10.1038/s41467-021-22180-6

Ravenscroft TA, Janssens J, Lee PT, Tepe B, Marcogliese PC, Makhzami S, Holmes TC, Aerts S, Bellen HJ. 2020. Drosophila voltage-gated sodium channels are only expressed in active neurons and are localized to distal axonal initial segment-like domains. *J Neurosci* **40**:7999–8024. doi:10.1523/JNEUROSCI.0142-20.2020

Reim K. 2016. ComplexinsThe Curated Reference Collection in Neuroscience and Biobehavioral Psychology. Elsevier Science Ltd. pp. 1–7. doi:10.1016/B978-0-12-809324-5.02507-4

Root CM, Masuyama K, Green DS, Enell LE, Nassel DR, Lee CH, Wang JW. 2008. A presynaptic gain control mechanism fine-tunes olfactory behavior. *Neuron* **59**:311–321. doi:10.1016/j.neuron.2008.07.003

Rotman Z, Klyachko VA. 2013. Role of synaptic dynamics and heterogeneity in neuronal learning of temporal code. *J Neurophysiol* **110**:2275–2286. doi:10.1152/jn.00454.2013

Rozenfeld E, Lerner H, Parnas M. 2019. Muscarinic Modulation of Antennal Lobe GABAergic Local Neurons Shapes Odor Coding and Behavior. *Cell Rep* **29**:3253–3265. doi:10.1016/j.celrep.2019.10.125

Sanyal S. 2009. Genomic mapping and expression patterns of C380, OK6 and D42 enhancer trap lines in the larval nervous system of Drosophila. *Gene Expr Patterns* **9**:371–380. doi:10.1016/J.GEP.2009.01.002

Scholz N, Ehmann N, Sachidanandan D, Imig C, Cooper BH, Jahn O, Reim K, Brose N, Meyer J, Lamberty M, Altrichter S, Bormann A, Hallermann S, Pauli M, Heckmann M, Stigloher C, Langenhan T, Kittel RJ. 2019. Complexin cooperates with Bruchpilot to tether synaptic vesicles to the active zone cytomatrix. *J Cell Biol* **218**:1011–1026. doi:10.1083/jcb.201806155

Schreiber S, Fellous JM, Whitmer D, Tiesinga P, Sejnowski TJ. 2003. A new correlation-based measure of spike timing reliability. *Neurocomputing* **52**–**54**:925–931. doi:10.1016/s0925-2312(02)00838-x

Seelig JD, Chiappe ME, Lott GK, Dutta A, Osborne JE, Reiser MB, Jayaraman V. 2010. Two-photon calcium imaging from head-fixed Drosophila during optomotor walking behavior. *Nat Methods* **7**:535–540. doi:10.1038/nmeth.1468

Shang Y, Claridge-Chang A, Sjulson L, Pypaert M, Miesenböck G. 2007. Excitatory Local Circuits and Their Implications for Olfactory Processing in the Fly Antennal Lobe. *Cell*. doi:10.1016/j.cell.2006.12.034

Stewart BAA, Atwood HLL, Renger JJJ, Wang J, Wu C-FF. 1994. Improved stability of Drosophila larval neuromuscular preparations in haemolymph-like physiological solutions. *J Comp Physiol A* **175**:179–191. doi:10.1007/BF00215114

Stocker RF, Heimbeck G, Gendre N, de Belle JS. 1997. Neuroblast ablation in Drosophila P[GAL4] lines reveals origins of olfactory interneurons. *J Neurobiol* **32**:443–56.

Stopfer M, Jayaraman V, Laurent G. 2003. Intensity versus identity coding in an olfactory system. *Neuron* **39**:991–1004.

Südhof TC. 2012. The presynaptic active zone. *Neuron*. doi:10.1016/j.neuron.2012.06.012

Tanaka NK, Endo K, Ito K. 2012. Organization of antennal lobe-associated neurons in adult Drosophila melanogaster brain. *J Comp Neurol* **520**:4067–4130. doi:10.1002/cne.23142

Tiesinga P, Fellous JM, Sejnowski TJ. 2008. Regulation of spike timing in visual cortical circuits. *Nat Rev Neurosci*. doi:10.1038/nrn2315

Trimbuch T, Rosenmund C. 2016. Should I stop or should I go? The role of complexin in neurotransmitter release. *Nat Rev Neurosci*. doi:10.1038/nrn.2015.16

Tsodyks M V, Markram H. 1997. The neural code between neocortical pyramidal neurons depends. *Proc Natl Acad Sci* **94**:719–723.

Vosshall LB, Amrein H, Morozov PS, Rzhetsky A, Axel R. 1999. A Spatial Map of Olfactory Receptor Expression in the Drosophila Antenna. *Cell* **96**:725–736. doi:10.1016/S0092-8674(00)80582-6

Vosshall LB, Wong AM, Axel R. 2000. An olfactory sensory map in the fly brain. *Cell* **102**:147–159. doi:10.1016/S0092-8674(00)00021-0

Walter AM, Böhme MA, Sigrist SJ. 2018. Vesicle release site organization at synaptic active zones. *Neurosci Res*. doi:10.1016/j.neures.2017.12.006

Wang HP, Spencer D, Fellous JM, Sejnowski TJ. 2010. Synchrony of thalamocortical inputs maximizes cortical reliability. *Science (80-)* **328**:106–109. doi:10.1126/science.1183108

Wilson RI, Laurent G. 2005. Role of GABAergic inhibition in shaping odor-evoked spatiotemporal patterns in the Drosophila antennal lobe. *J Neurosci* **25**:9069–9079. doi:10.1523/JNEUROSCI.2070-05.2005

Winther ÅME, Vorontsova O, Rees KA, Näreoja T, Sopova E, Jiao W, Shupliakov O. 2015. An endocytic scaffolding protein together with Synapsin regulates synaptic vesicle clustering in the drosophila neuromuscular junction. *J Neurosci* **35**:14756–14770. doi:10.1523/JNEUROSCI.1675-15.2015

Yang H, Xu-Friedman MA. 2013. Stochastic properties of neurotransmitter release expand the dynamic range of synapses. *J Neurosci* **33**:14406–14416. doi:10.1523/JNEUROSCI.2487-13.2013

Youden WJ. 1950. Index for rating diagnostic tests. *Cancer* **3**:32–35. doi:10.1002/1097-0142(1950)3:1<32::AID-CNCR2820030106>3.0.CO;2-3

Yu J, Qian H, Wang JH. 2012. Upregulation of transmitter release probability improves a conversion of synaptic analogue signals into neuronal digital spikes. *Mol Brain* **5**:26. doi:10.1186/1756-6606-5-26

Zador A. 1998. Impact of synaptic unreliability on the information transmitted by spiking neurons. *J Neurophysiol* **79**:1219–1229. doi:10.1152/jn.1998.79.3.1219

Figure 1

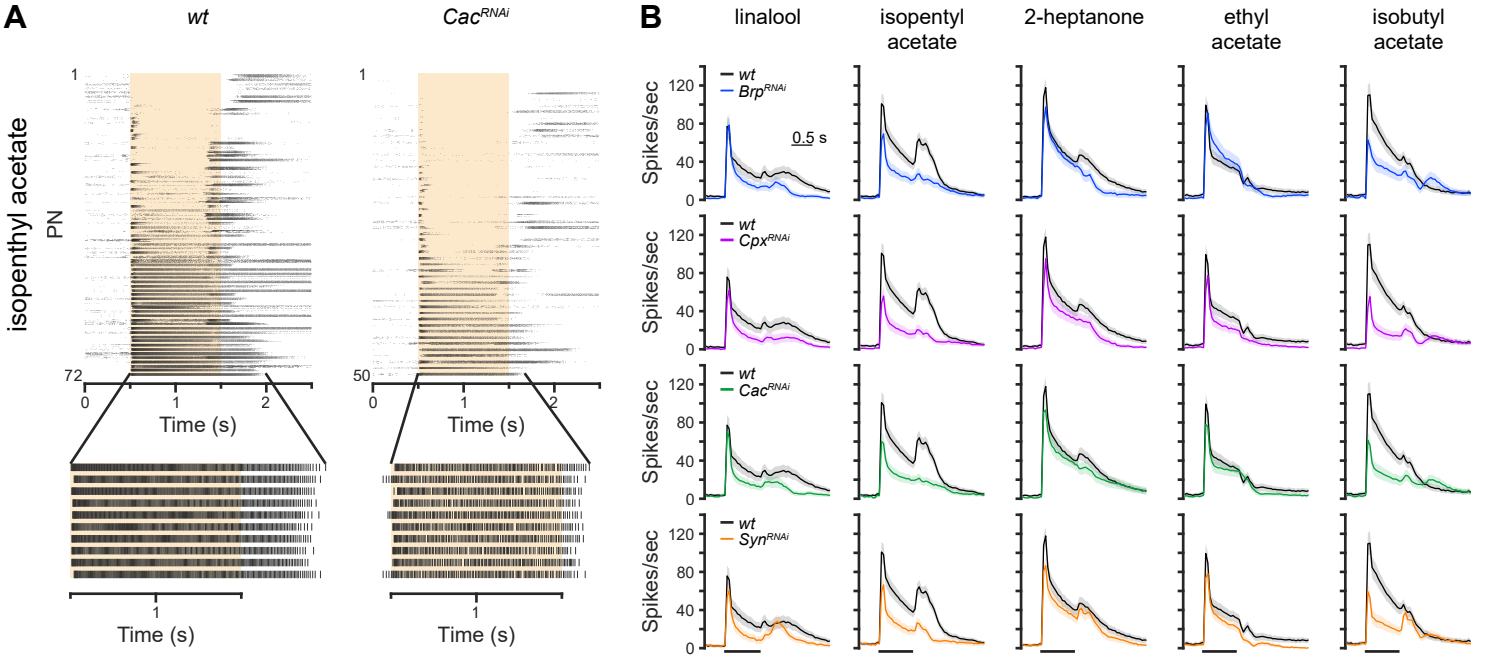
A
wt
Cac^RNAi
isopenthyl acetate
PN
1
72
50
0
1
2
Time (s)
B
linalool
isopentyl acetate
2-heptanone
ethyl acetate
isobutyl acetate
Spikes/sec
120
80
40
0
0.5 s
wt
Brp^RNAi
Cpx^RNAi
Cac^RNAi
Syn^RNAi

Figure 1: PN odor responses are shaped by the presynaptic protein composition of ORNs

A. *Top*, Raster plot of PN population odor responses to isopenthyl acetate (a final odor dilution of $5X10^{-2}$ was used) in *wt* flies (left, n=72 flies) and Cac^{RNAi} in ORNs (right, n=50 flies). Each neuron was presented with 10 repetitions of the olfactory stimulus (1 s). *Bottom*, the 10 repetitions of a single PN are presented. The shaded area indicates the odor stimulus.

B. Peristimulus time histogram (PSTH) of PN population responses to five odors examined as indicated (shaded areas represent SEM, odor pulse is labeled with a black bar) obtained from recordings as in panel A. Spike trains were binned using a 50 ms time bin. Knockdown of the AZ proteins Brp (blue), Cpx (purple), Cac (green), and the vesicle-associated protein Syn (orange) in ORNs resulted in decreased PN odor responses. A final odor dilution of $5X10^{-2}$ was used (n=48-72 flies). *Orco-GAL4* was used to drive the RNAi constructs and *GH146-QF* drove *QUAS-GFP*.

Figure 2

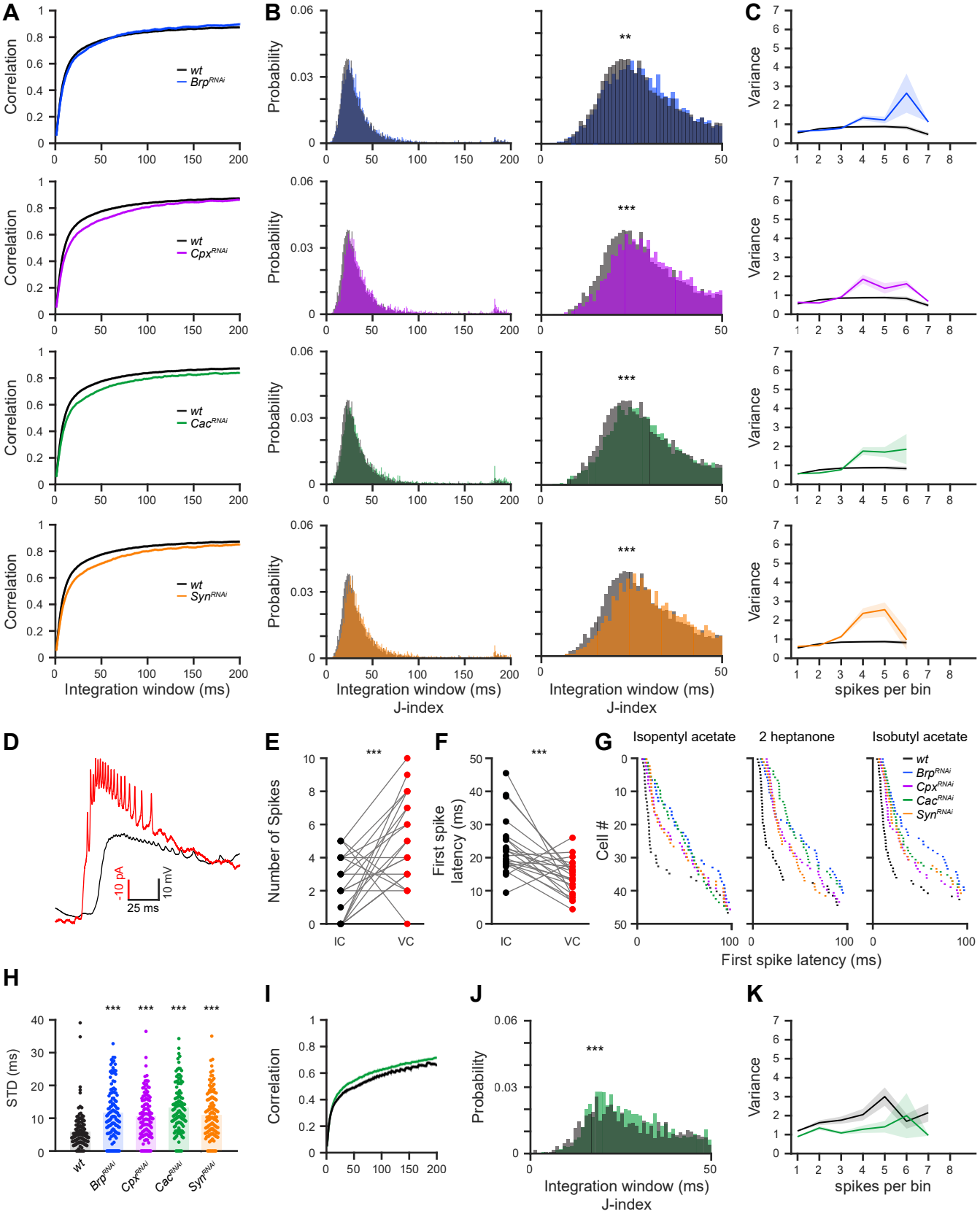
A
B
C
Correlation
Probability
Variance
wt
Brp^RNAi
Cpx^RNAi
Cac^RNAi
Syn^RNAi
Integration window (ms)
J-index
spikes per bin
**
***
D
-10 pA
10 mV
25 ms
E
Number of Spikes
IC
VC
F
First spike latency (ms)
G
Isopentyl acetate
2 heptanone
Isobutyl acetate
Cell #
First spike latency (ms)
H
STD (ms)
I
J
K

Figure 2: Presynaptic protein knockdown reduces neuronal coding reliability at high firing rates

A. Temporal reliability analysis. Pairwise correlations for each odor-neuron combination were pooled across all odors for data in Figure S1 with a final odor dilution of $5X10^{-2}$. Non-overlapping windows from 1 to 200 ms were used. RNAi of AZ proteins in ORNs reduces correlation values.

B. *Left*, the J-index (curve saturation point) was calculated for each odor-neuron combination and pooled across all odors for data in Figure S1. *Right*, Left curves are presented at a larger scale. RNAi of ORN AZ proteins shifts the optimal temporal integration window of PNs as evident by a larger integration window spread (left) and a peak shift of ~10 ms (right).

C. Firing-rate reliability analysis for data in Figure S1. Spike trains were binned using 20 ms windows. Spike count and variability were calculated for each bin and pooled across neurons, odors, and time. Increased rate variability is observed for high firing rates.

D. Example traces of recordings performed in current clamp (IC, black) and in voltage clamp (VC, red). Note, the VC trace is inverted for presentation purposes.

E. PN firing-rate during the first 25 ms of the response to isopentyl acetate in current clamp (IC, black) vs. voltage clamp (VC, red). Each dot represents an individual fly (n=22). The VC configuration enabled detection of more action potentials.

F. First spike latency of PNs in response to isopentyl acetate in IC (black) vs. VC (red). Dots represent individual flies (n=22).

G. First spike latency of PNs in response to the indicated odors for *wt* and RNAi flies (n=50-55). Each dot represent the mean first spike latency for 10 trials of a given neuron. Data were obtained in VC configuration and PNs that did not spike within 100ms after stimulus onset were omitted.

H. First spike jitter of PN odor responses, pooled across all odors, for *wt* and RNAi flies (n=50-55).

I-K. Temporal reliability (H), J-index (I), and firing-rate reliability (J) for an odor concentration of $5X10^{-4}$ pooled across all odors (isopenthyl acetate, isobutyl acetate and linalool). *Orco-GAL4*

drove *UAS-Cac*^{RNAi} in ORNs and *GH146-QF* drove *QUAS-GFP* in PNs. No increase in integration time was observed for low odor concentration (n=49-50).

For all panels, ** $p<0.01$, *** $p<0.001$, two-sample or paired two-sample t-test, see table S1.

Figure 3

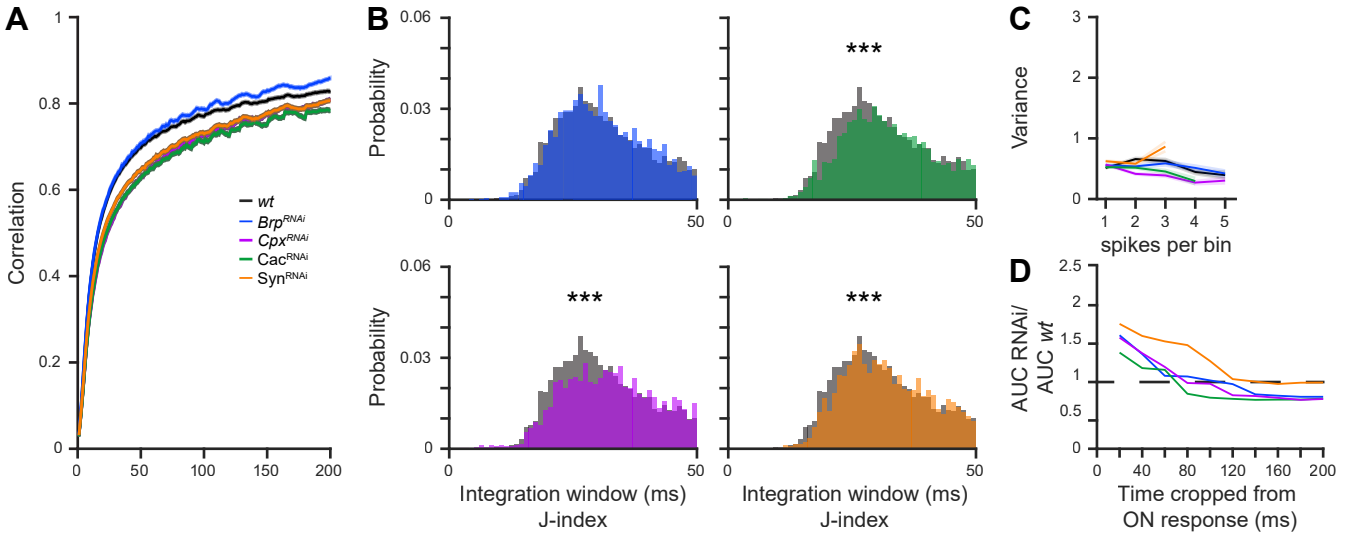
A
Correlation
wt
Brp^RNAi
Cpx^RNAi
Cac^RNAi
Syn^RNAi
B
Probability
***
Integration window (ms)
J-index
C
Variance
spikes per bin
D
AUC RNAi/
AUC wt
Time cropped from
ON response (ms)

Figure 3: Presynaptic protein knockdown reduces neural rate coding reliability in the initial phase of the odor response

A. Temporal reliability analysis for data in Figure S1. Removing the first 200 ms of the odor response leads to an overall decrease in correlation.

B. J-index analysis for data in Figure S1 without the first 200 ms of the odor response. A shift of the peak of the curve is observed for the sustained odor response in RNAi lines.

C. Firing-rate reliability analysis for data in Figure S1 without the first 200 ms of the odor response. Contrary to the increased variation observed for the entire odor response (Figure 2C), the RNAi lines did not increase the variability for the sustained odor response although high firing-rates were still obtained.

D. The ratio between the area under the curve (AUC) of the rate code variability in RNAi lines relative to *wt*. The initial response was progressively cropped from the analysis. The difference in rate code variation of *wt* and RNAi flies gradually decreases over the first 200 ms of the odor response.

Figure 4

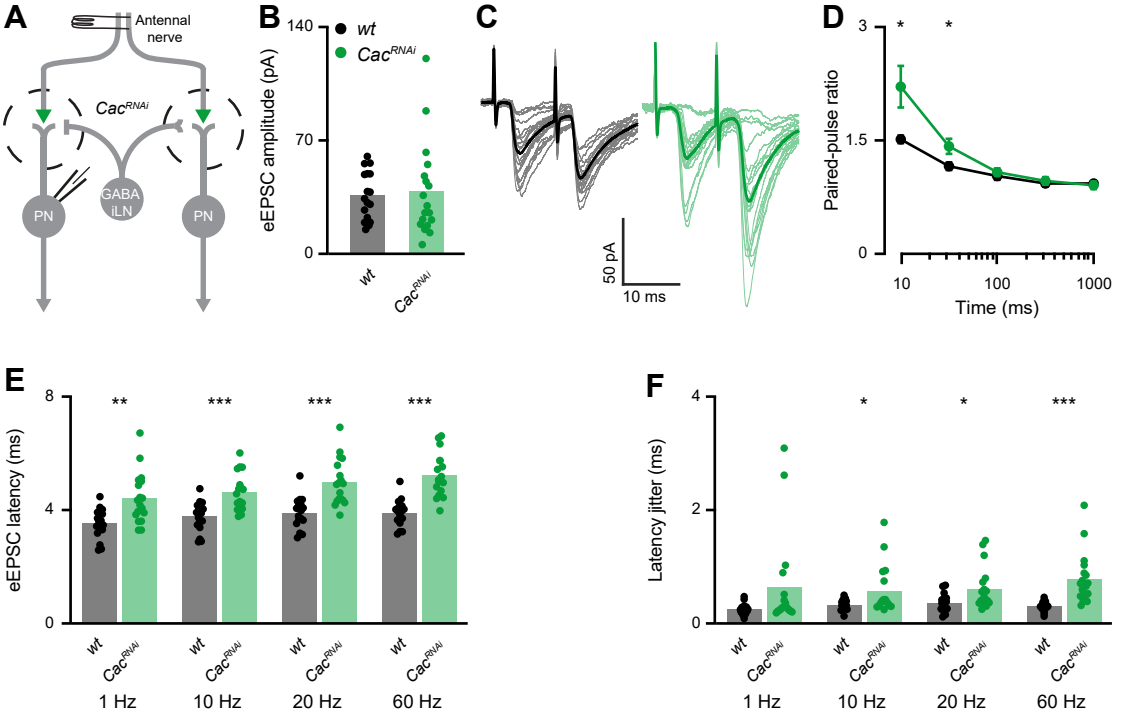
A
Antennal nerve
Cac^RNAi
GABA iLN
PN
PN
B
wt
Cac^RNAi
eEPSC amplitude (pA)
140
70
0
wt
Cac^RNAi
C
50 pA
10 ms
D
Paired-pulse ratio
3
1.5
0
*
*
10
100
1000
Time (ms)
E
eEPSC latency (ms)
8
4
0
**
***
***
***
wt
Cac^RNAi
1 Hz
10 Hz
20 Hz
60 Hz
F
Latency jitter (ms)
4
2
0
*
*
***
wt
Cac^RNAi
1 Hz
10 Hz
20 Hz
60 Hz

Figure 4: Presynaptic Cac knockdown reduces the temporal precision of synaptic transmission

A. Experimental scheme. *UAS-Cac*^{RNAi} was expressed in ORNs using *Orco-GAL4* and whole-cell patch clamp recordings were made from PNs labeled by the *GH146-QF* driver line. The antennal nerve was stimulated with a suction electrode.

B. The average eEPSC amplitude was unaltered by *Cac*^{RNAi} (1 Hz stimulation frequency; *Orco-Gal4* driver, *wt* n=17 and *Cac*^{RNAi} n=18 flies).

C. Examples traces of eEPSC evoked by paired pulse stimulation with an interpulse interval of 10ms.

D. Quantification of the paired-pulse ratio at different inter-stimulus intervals (10ms, 30ms, 100ms, 300ms and 1000ms). *Cac*^{RNAi} significantly increased paired-pulse facilitation at short interpulse intervals (*wt*, n=20-22; *Cac*^{RNAi}, n=24-28 flies). Error bars represent SEM. * $p<0.05$, two-sample t-test, see table S1.

E, F. Average eEPSC latencies (**E**) and average eEPSC jitter (**F**) at 1, 10, 20, and 60 Hz stimulation for *wt* (n=17) and *Cac*^{RNAi} (n=18) flies. A significant increase was observed for all tested stimulation frequencies (except of jitter at 1 Hz). *** $p<0.001$, ** $p<0.01$, * $p<0.05$, two-sample t-test, see table S1.

Figure 5

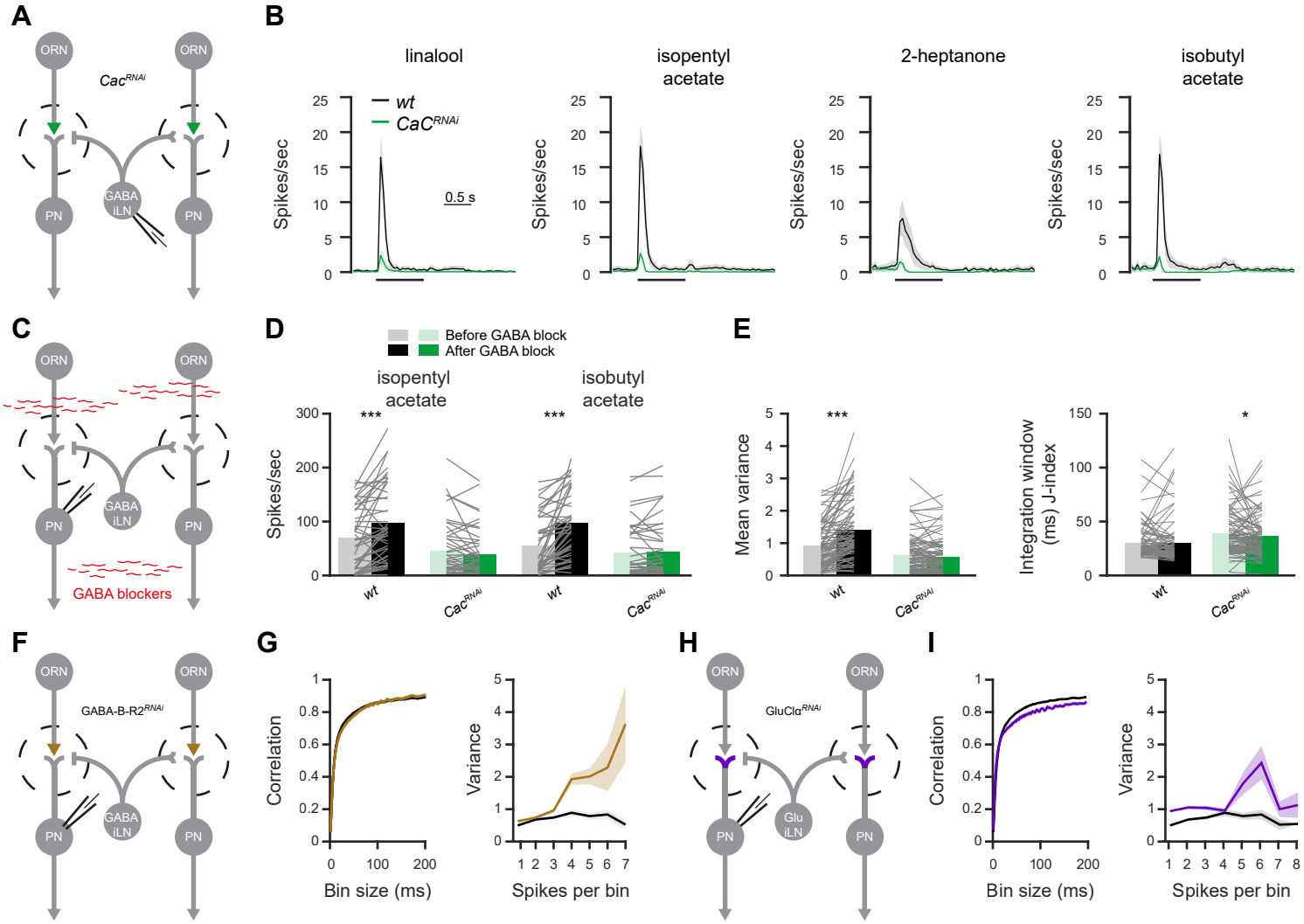
A
ORN
ORN
Cac^RNAi
GABA iLN
PN
PN
B
linalool
isopentyl acetate
2-heptanone
isobutyl acetate
wt
CaC^RNAi
Spikes/sec
0.5 s
C
GABA blockers
D
Before GABA block
After GABA block
isopentyl acetate
isobutyl acetate
***
wt
Cac^RNAi
E
Mean variance
Integration window (ms) J-index
*
F
GABA-B-R2^RNAi
G
Correlation
Bin size (ms)
Variance
Spikes per bin
H
GluClα^RNAi
Glu iLN
I

Figure 5: Monosynaptic effects underlie temporal reliability whereas circuit effects underlie rate code reliability

A. Experimental scheme. *Cac*^{RNAi} was driven in ORNs using *Orco-GAL4.* Whole-cell patch recordings were made from iLNs labeled with the *449-QF* driver line.

B. PSTH of the iLN population response to four odors examined as indicated (shaded areas represent SEM, the odor pulse is labeled with a black bar). Cac knockdown resulted in an almost complete abolishment of iLN odor responses (final odor dilution of $5X10^{-2}$; n=49-50 flies).

C. Experimental scheme. GABA receptors blockers (100 µM CGP54626 and 250 µM picrotoxin) were applied by bath perfusion. Whole-cell patch recordings were made from PNs labeled with the *GH146-QF* driver line.

D. Mean firing rate during the odor response. Application of GABA blockers significantly increased *wt* firing rates but had no effect on *Cac*^{RNAi}. *Orco-GAL4* drove *UAS-Cac*^{RNAi} and *GH146-QF* drove *QUAS-GFP* (n = 45-48 flies, *** $p < 0.001$, paired two-sample t-test, see table S1).

E. *Left.* Temporal integration window and *right*, firing-rate reliability analysis for *wt* and *Cac*^{RNAi} flies before and after the application of GABA receptors blockers (100 µM CGP54626, and 250 µM picrotoxin). The data were pooled for the presentation of two odors (isopentyl acetate and isobutyl acetate) and across all firing-rates (n=45-48 flies).

F. Experimental scheme. An RNAi construct against the GABA-B-R2 receptor was expressed in ORNs using *Orco-GAL4*. Whole-cell patch recordings were made from PNs labeled with the *GH146-QF* driver line.

G. *Left*. Temporal integration window and *right*, firing-rate reliability analysis for *wt* and *GABA-B-R2*^{RNAi} flies (brown). The data were pooled for the presentation of two odors (isopentyl acetate and isobutyl acetate) and across all firing-rates (n=50-72 flies).

H. Experimental scheme. An RNAi construct against the GluClα receptor was expressed in PNs using *GH146-GAL4.* Whole-cell patch recordings were made from PNs.

I. *Left*. Temporal integration window and *right*, firing-rate reliability analysis for *wt* and GluClα^{RNAi} flies (purple). The data were pooled for the presentation of two odors (isopentyl acetate and isobutyl acetate) and across all firing-rates (n=50-72 flies).

For all panels, * $p<0.05$, ** $p<0.01$, *** $p<0.001$, two-sample or paired two-sample t-test, see table S1.

Figure 6

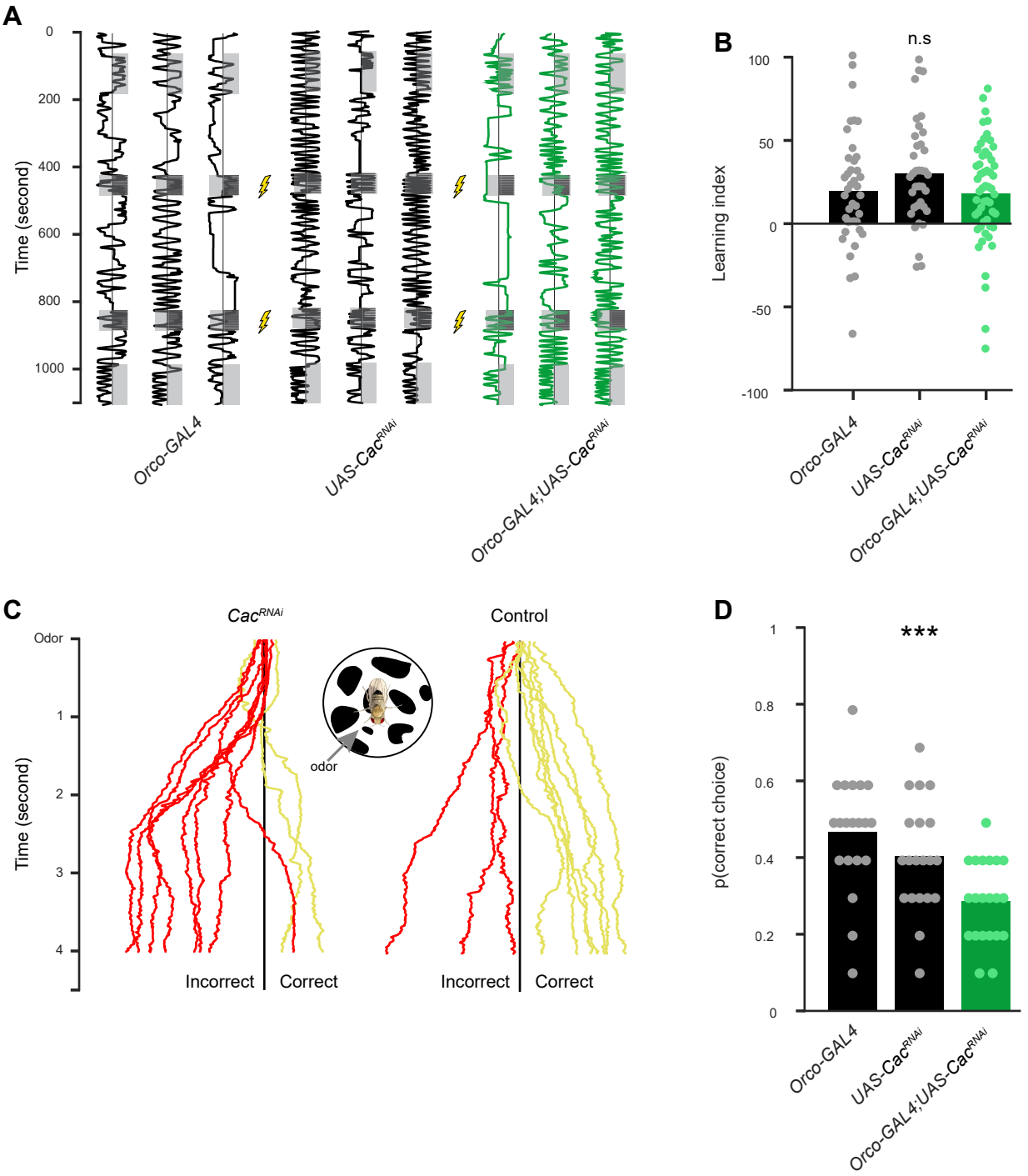
A
Time (second)
0
200
400
600
800
1000
Orco-GAL4
UAS-Cac^RNAi
Orco-GAL4;UAS-Cac^RNAi
B
n.s
Learning index
100
50
0
-50
-100
Orco-GAL4
UAS-Cac^RNAi
Orco-GAL4;UAS-Cac^RNAi
C
Cac^RNAi
Control
Odor
Time (second)
1
2
3
4
odor
Incorrect
Correct
Incorrect
Correct
D
***
p(correct choice)
1
0.8
0.6
0.4
0.2
0
Orco-GAL4
UAS-Cac^RNAi
Orco-GAL4;UAS-Cac^RNAi

Figure 6: Cac knockdown reduces behavioral reliability

A. Experimental scheme for the learning paradigm. Flies were constrained in a linear chamber with isopentyl acetate presented on one side (gray). For pairing with an electric shock, the odor was presented on both sides of the chamber. Examples of single fly trajectories are shown.

B. Learning performance for prolonged odor exposure. No significant differences in the learning index were observed between the parental controls and Cac^{RNAi} in ORNs. Each dot represents a single fly (n=37-54, one-way ANOVA, see table S1).

C. Trained flies were tested in an assay where flies walked on a ball and the shock-paired odor was presented from the indicated side. Ten one second odor trials were presented as in Figure 1. Examples for single fly trajectories along the virtual X-axis are presented. Choice was classified as correct (yellow) if the mean X-axis position following the odor presentation was rightward of the X-axis midline (black line) and incorrect (red) otherwise.

D. Behavioral reliability measure. The behavioral reliability measure was defined as the probability of correctly classifying the shock-paired odor. Cac knockdown in ORNs reduces the behavioral reliability compared to the parental controls. Each dot represents a single fly (n=20-21, *** $p<0.001$, one-way ANOVA, see table S1).

Supplementary Information

Molecular Mechanisms of Neurotransmitter Release Control Distinct Features of Sensory Coding Reliability

Eyal Rozenfeld, Nadine Ehmann, Julia E. Manoim, Robert J. Kittel and Moshe Parnas

Figure S1

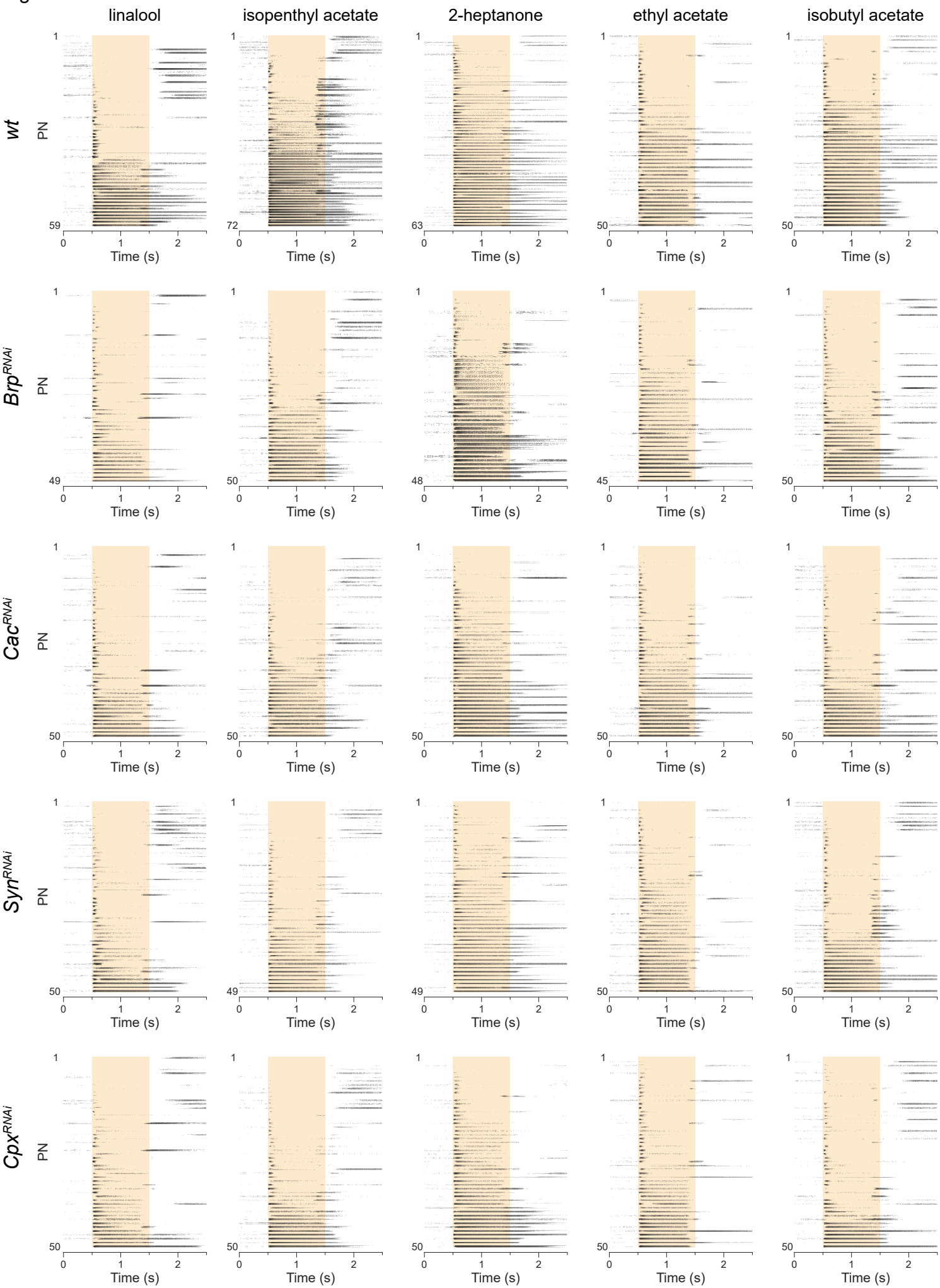
linalool
isopenthyl acetate
2-heptanone
ethyl acetate
isobutyl acetate
wt
Brp^RNAi
Cac^RNAi
Syn^RNAi
Cpx^RNAi
PN
Time (s)
1
59
72
63
50
49
48
45
0
1
2

Figure S1: PN population responses to odor stimulation

Raster plot of PN population responses to five odors as indicated (final odor dilution of $5X10^{-2}$) in *wt* flies and RNAi lines. Each neuron was presented with 10 repetitions of the olfactory stimulus. *Orco-GAL4* drove either *UAS-BRP*^{RNAi}, *UAS-Cpx*^{RNAi}, *UAS-Cac*^{RNAi} or *UAS-Syn*^{RNAi} in ORNs and *GH146-QF* drove *QUAS-GFP* (n=45-72).

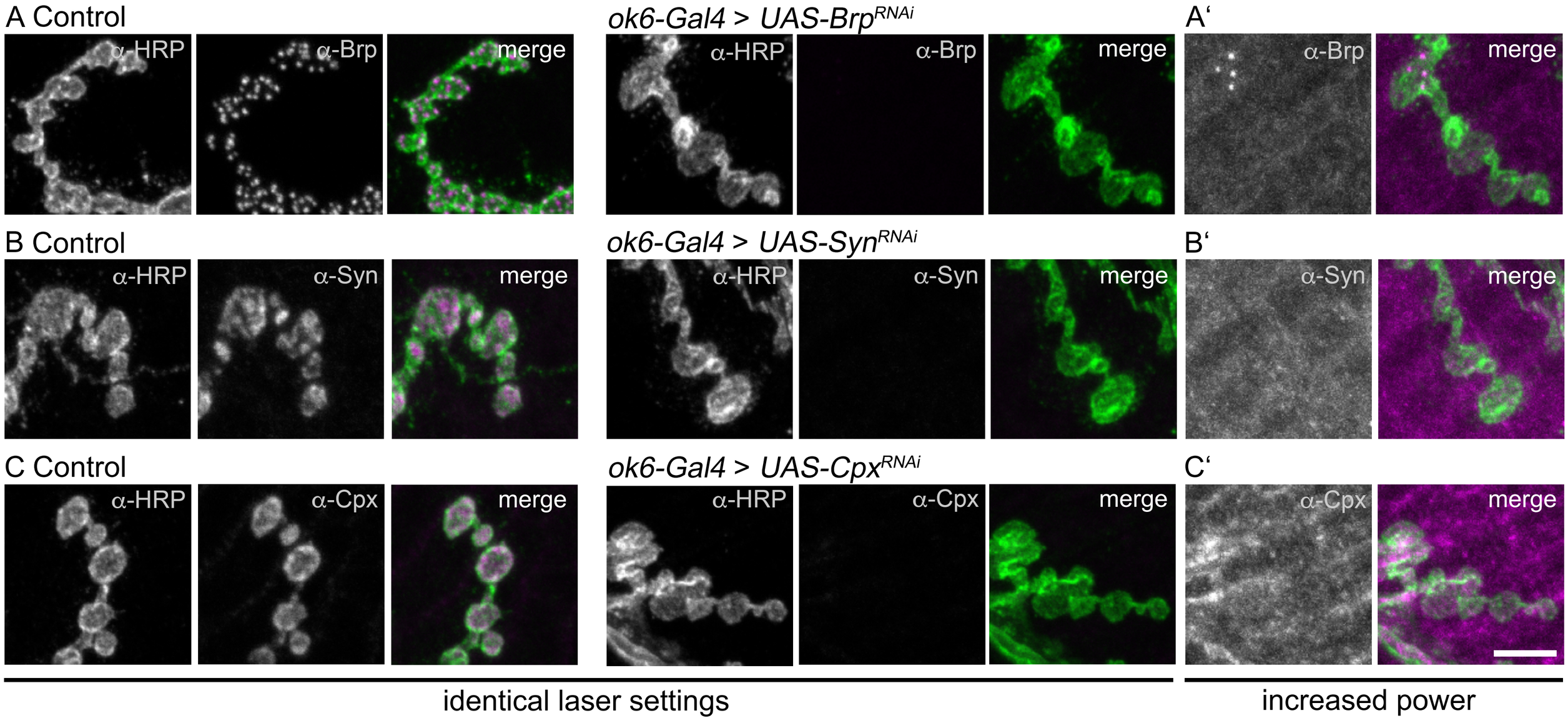
A Control
α-HRP
α-Brp
merge
ok6-Gal4 > UAS-Brp^RNAi
α-HRP
α-Brp
merge
A‘
α-Brp
merge
B Control
α-HRP
α-Syn
merge
ok6-Gal4 > UAS-Syn^RNAi
α-HRP
α-Syn
merge
B‘
α-Syn
merge
C Control
α-HRP
α-Cpx
merge
ok6-Gal4 > UAS-Cpx^RNAi
α-HRP
α-Cpx
merge
C‘
α-Cpx
merge
identical laser settings
increased power

Figure S2: Immunohistochemical confirmation of RNAi efficiency

Maximal projections of confocal stacks show strong reduction of Brp (**A**), Syn (**B**) and Cpx (**C**) in motoneuron boutons following knockdown with the respective RNAi construct (middle panel; *ok6-Gal4 > UAS-Brp*^{RNAi}*, ok6-Gal4 > UAS-Syn*^{RNAi}*, ok6-Gal4 > UAS-Cpx*^{RNAi}; controls: left panel). Anti-HRP (horseradish peroxidase) was employed to stain neuronal membranes. **A'**, **B'** and **C'** show the same positions depicted in middle panel with increased laser power. Scale bar: 5µm.

Figure S3

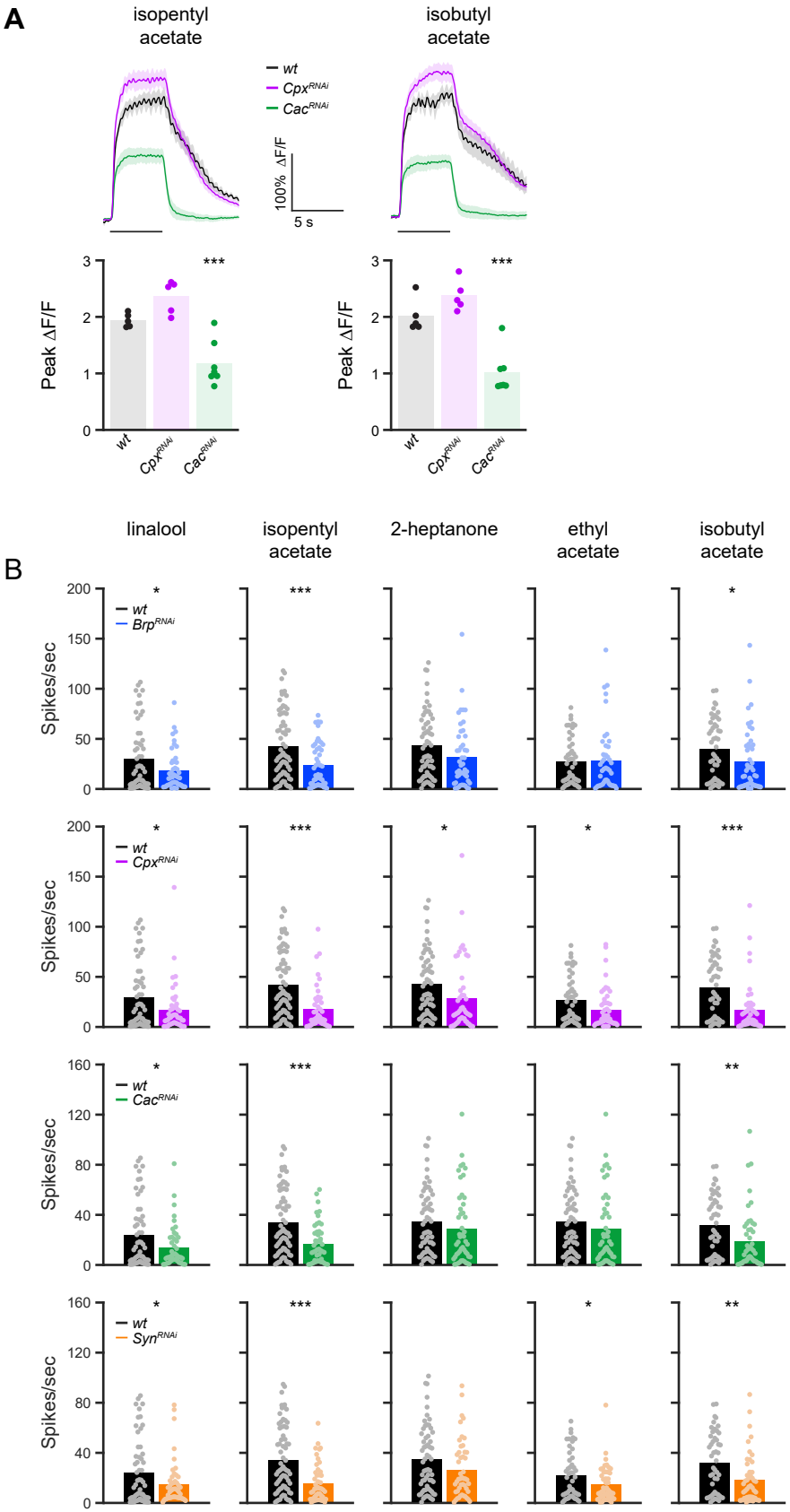
A
isopentyl acetate
isobutyl acetate
wt
Cpx^RNAi
Cac^RNAi
100% ΔF/F
5 s
Peak ΔF/F
***
B
linalool
isopentyl acetate
2-heptanone
ethyl acetate
isobutyl acetate
Spikes/sec
wt
Brp^RNAi
Cpx^RNAi
Cac^RNAi
Syn^RNAi
*
**
***

Figure S3: Knockdown of presynaptic proteins differentially affects ORNs and reduces odor-stimulated PN firing rates

A. *Top*, averaged traces ± SEM (shading) of odor responses (as indicated, odor pulse is labeled with a black bar) obtained from a single plane of the entire AL for *wt* or RNAi flies. *Orco-GAL4* drove either *UAS-Cpx*^{RNAi} or *UAS-Cac*^{RNAi} along with *UAS-GCaMP6f*. *Bottom*, peak ∆F/F during odor responses for the traces presented in the *top* panel. As expected, a significant decrease in Ca^{2+} signals was observed only for *Cac*^{RNAi}. Color-coding as in Figure 1. (n = 5-7 flies, ** $p < 0.01$, ** $p < 0.001$, Two-sample t-test, see table S1).

B. Mean firing rate of PNs in response to five odors as indicated (final odor dilution of $5X10^{-2}$) for *wt* flies and for ORN RNAi lines of presynaptic proteins as indicated. Each data point shows the average of 10 responses to a 1 s odor stimulus and 1 s following the odor stimulus. *Orco-GAL4* drove either *UAS-Brp*^{RNAi}, *UAS-Cpx*^{RNAi}, *UAS-Cac*^{RNAi} or *UAS-Syn*^{RNAi} in ORNs and *GH146-QF* drove *QUAS-GFP*. For most RNAi flies and most odors significant decrease in firing rate was observed. Color-coding is as in Figure 1. (n=45-72, * $p<0.05$, ** $p<0.01$, *** $p<0.001$, Two-sample t-test, see table S1).

Figure S4

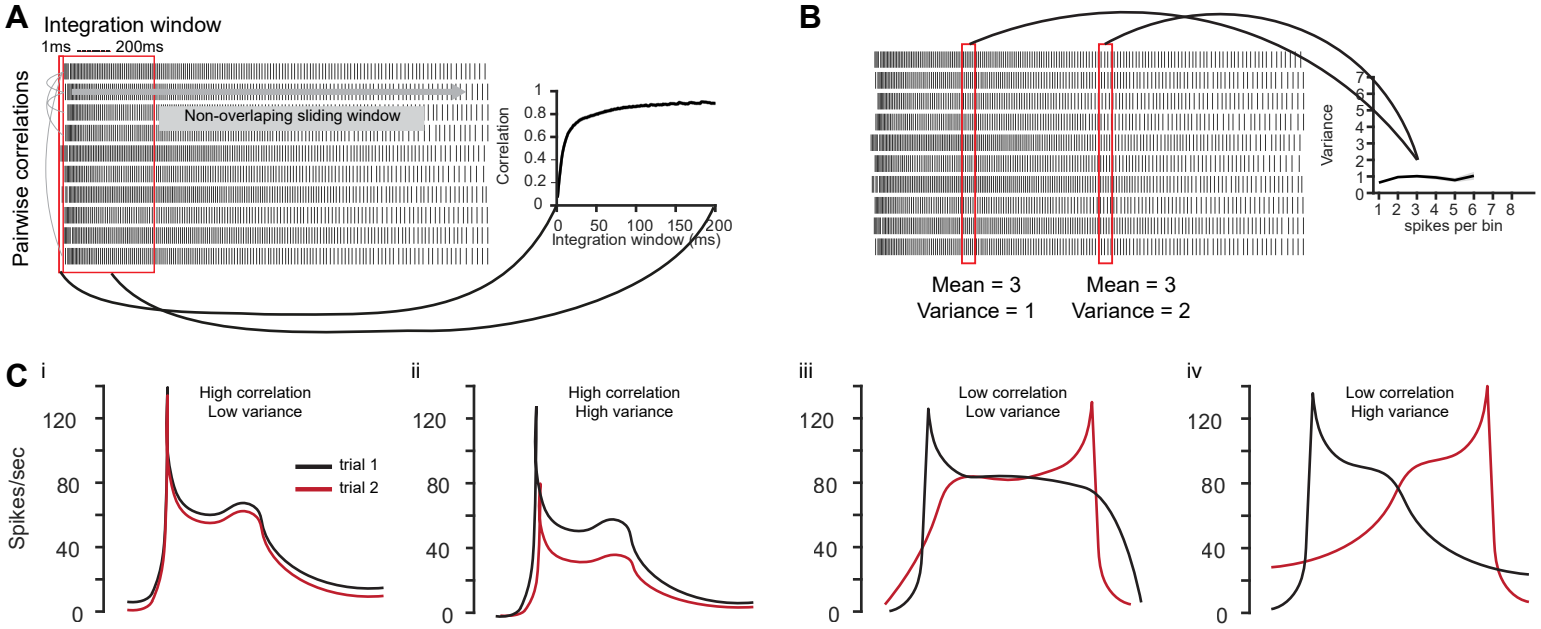
A
Integration window
1ms 200ms
Pairwise correlations
Non-overlaping sliding window
Correlation
Integration window (ms)
B
Variance
spikes per bin
Mean = 3
Variance = 1
Mean = 3
Variance = 2
C
i
High correlation
Low variance
trial 1
trial 2
ii
High correlation
High variance
iii
Low correlation
Low variance
iv
Low correlation
High variance
Spikes/sec

Figure S4: Graphical description of the reliability analysis

A. Temporal reliability analysis. Pairwise correlations were performed between the 10 repetitions of each odor-neuron combination. Correlations were calculated using increasing, non-overlapping integration windows from 1 to 200 ms with 1 ms intervals. The 45 pairwise correlation values for each condition (i.e. PN and odor) were averaged to a single correlation value for this condition. All correlation values for all PNs and odors were pooled to yield the correlation curve on the right.

B. Firing rate reliability analysis. Spike trains were binned using 20 ms windows. The number of spikes and variability was calculated for each individual bin. The mean variance value for all bins having the same number of spikes is presented on the variance curve on the right. Variance values are pooled across neurons, odors and time.

C. Temporal reliability analysis and firing rate reliability analysis capture different aspects of trial-to-trial coding reliability. Correlation captures the general shape of the PSTH regardless of momentary changes in firing rate at a given point in time (i and ii). Inter trial variability captures the momentary changes in firing rates regardless of the PSTH temporal dynamics (ii and iv).

Figure S5

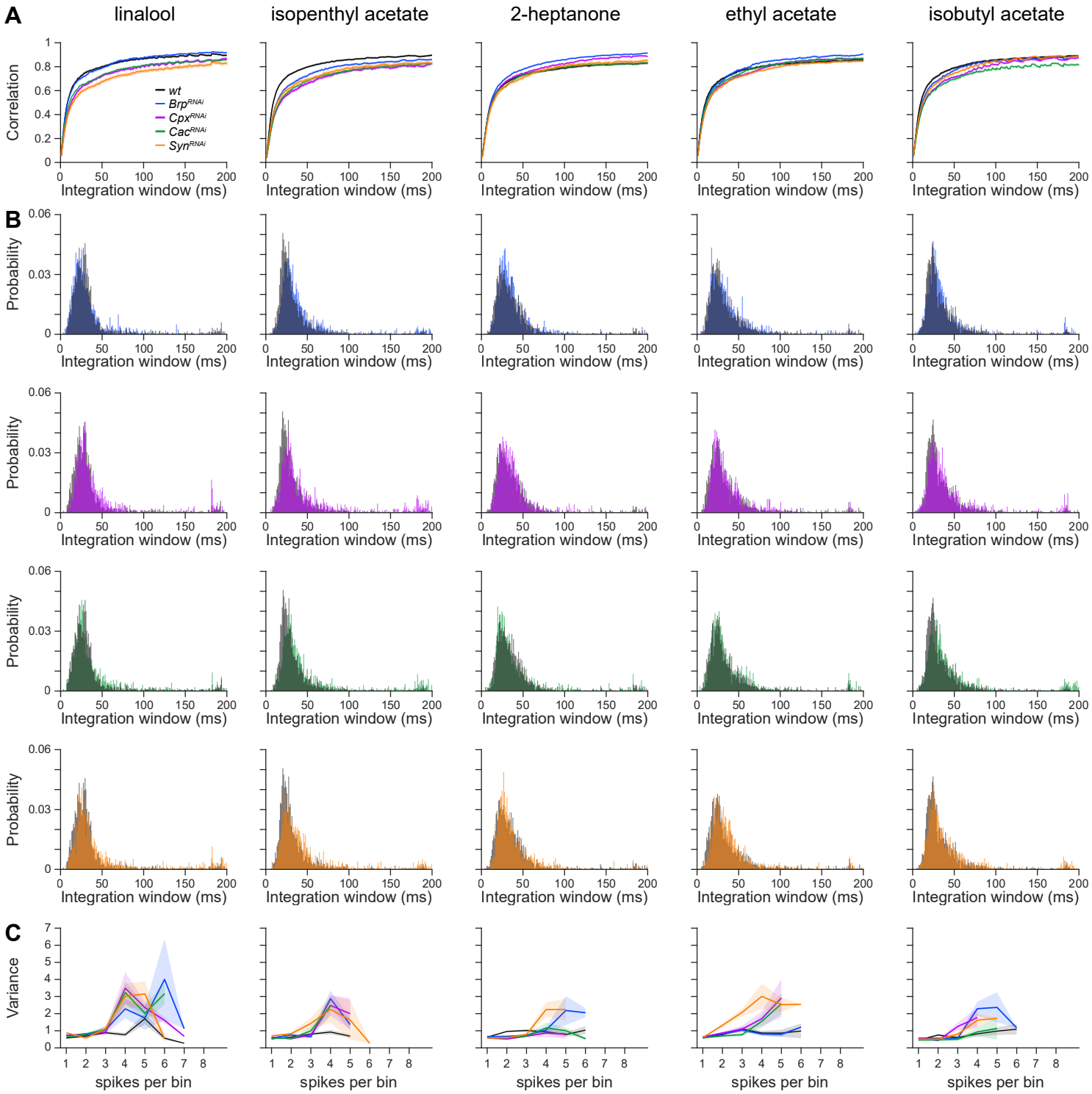
A
linalool
isopenthyl acetate
2-heptanone
ethyl acetate
isobutyl acetate
Correlation
wt
Brp^RNAi
Cpx^RNAi
Cac^RNAi
Syn^RNAi
Integration window (ms)
B
Probability
C
Variance
spikes per bin

Figure S5: Single odor analyses of response reliability

A. Temporal reliability analysis as performed in Figure 2A but for single odors as indicated. Data obtained from Figure 1 and Figure S1. For all odors, a final odor dilution of $5X10^{-2}$ was used. Color-coding is as in Figure 1.

B. The J-index analysis as performed in Figure 2B but for single odors as indicated. Data obtained from Figure 1 and Figure S1. For all odors, a final odor dilution of $5X10^{-2}$ was used. Color-coding is as in Figure 1.

C. Firing rate reliability analysis as performed in Figure 2C but for single odors as indicated. Data obtained from Figure 1 and Figure S1. For all odors, a final odor dilution of $5X10^{-2}$ was used. Color-coding as in Figure 1.

Figure S6

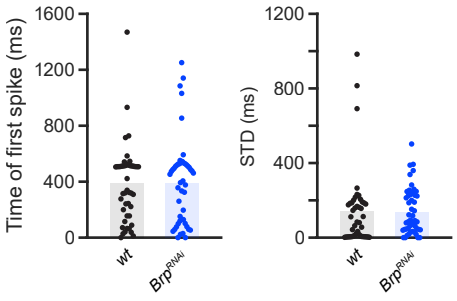
Time of first spike (ms)
1600
1200
800
400
0
wt
Brp^RNAi
STD (ms)
1200
800
400
0
wt
Brp^RNAi

Figure S6: Controls for first spike analysis

Analysis of the latency of the first spike (left) and jitter of the first spike (right) in PNs as performed in Figure 2G, H but in response to mock odor application (i.e. no odor was actually applied) for *wt* flies or Brp^{RNAi} in ORNs (n=50-55). Color-coding is as in Figure 1. No change in any parameter was observed.

Figure S7

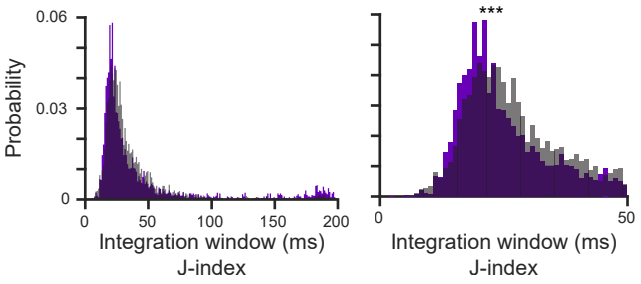
0.06
0.03
0
Probability
0
50
100
150
200
Integration window (ms)
J-index
***
0
50
Integration window (ms)
J-index

Figure S7: GluClα RNAi in PNs does not increase their integration window

Left, the J-index (curve saturation point) was calculated for each odor-neuron combination and pooled across the two odors for the data in Figure 5I. *Right*, Left curves are presented at a larger scale. GluClα knockdown in PNs did not increase their optimal temporal integration window. If at all, it slightly improved as reflected by a smaller integration window spread and a slight peak shift to the left.

Table S1: statistical analysis

Figure	data	Statistical method	comparison	P-value	Effect size	significance
Figure 2B	J-index probability *Brp*^{RNAi} all odors pooled	Two sample t-test	1. Control (N=12133) 2. *Brp*^{RNAi} (N=9842)	0.004	-0.038	**
	J-index probability *Cpx*^{RNAi} all odors pooled	Two sample t-test	1. Control (N=12133) 2. *Cpx*^{RNAi} (N=9746)	<0.001	-0.220	***
	J-index probability *Cac*^{RNAi} all odors pooled	Two sample t-test	1. Control (N=12133) 2. *Cac*^{RNAi} (N=9883)	<0.001	-0.211	***
	J-index probability *Syn*^{RNAi} all odors pooled	Two sample t-test	1. Control (N=12133) 2. *Syn*^{RNAi} (N=9883)	<0.001	-0.212	***
Figure 2E	Spike count IC vs. VC	Two sample paired t-test	1. IC (N=22) 2. VC (N=22)	0.001	-1.162	***
Figure 2F	First spike latency IC vs. VC	Two sample paired t-test	1. IC (N=22) 2. VC (N=22)	<0.001	1.265	***
Figure 2H	First spike jitter all odors pooled	Two sample t-test	1. Control (N=134) 2. *Brp*^{RNAi} (N=131)	<0.001	-0.864	***
	First spike jitter all odors pooled	Two sample t-test	1. Control (N=134) 2. *Cpx*^{RNAi} (N=135)	<0.001	-0.794	***
	First spike jitter all odors pooled	Two sample t-test	1. Control (N=134) 2. *Cac*^{RNAi} (N=127)	<0.001	-1.178	***
	First spike jitter all odors pooled	Two sample t-test	1. Control (N=134) 2. *Syn*^{RNAi} (N=132)	<0.001	-0.851	***
Figure 2J	J-index probability *Cac*^{RNAi} all odors pooled	Two sample t-test	1. Control (N=4198) 2. *Cac*^{RNAi} (N=4722)	<0.001	0.083	***
Figure 3B	J-index probability *Brp*^{RNAi} all odors pooled	Two sample t-test	1. Control (N=9803)	0.059	-0.029	n.s

			2. *Brp*^{RNAi} (N=7303)			
	J-index probability *Cpx*^{RNAi} all odors pooled	Two sample t-test	1. Control (N=9803) 2. *Cpx*^{RNAi} (N=7008)	<0.001	-0.229	***
	J-index probability *Cac*^{RNAi} all odors pooled	Two sample t-test	1. Control (N=9803) 2. *Cac*^{RNAi} (N=7156)	<0.001	-0.253	***
	J-index probability *Syn*^{RNAi} all odors pooled	Two sample t-test	1. Control (N=9803) 2. *Syn*^{RNAi} (N=7843)	<0.001	-0.192	***
Figure 4D	Paired-pulse ratio (10ms)	Two sample t-test	1. Control (N=20) 2. *Cac*^{RNAi} (N=24)	0.026	-0.683	*
	Paired-pulse ratio (30ms)	Two sample t-test	1. Control (N=21) 2. *Cac*^{RNAi} (N=24)	0.042	-0.614	*
Figure 4E	eEPSC latency – 1Hz	Two sample t-test	1. Control (N=17) 2. *Cac*^{RNAi} (N=18)	0.001	-1.185	**
	eEPSC latency – 10Hz	Two sample t-test	1. Control (N=17) 2. *Cac*^{RNAi} (N=17)	<0.001	-1.402	***
	eEPSC latency – 20Hz	Two sample t-test	1. Control (N=17) 2. *Cac*^{RNAi} (N=18)	<0.001	-1.518	***
	eEPSC latency – 60Hz	Two sample t-test	1. Control (N=17) 2. *Cac*^{RNAi} (N=18)	<0.001	-2.053	***
Figure 4F	eEPSC jitter – 1Hz	Two sample t-test	1. Control (N=17) 2. *Cac*^{RNAi} (N=18)	0.073	-0.611	n.s
	eEPSC jitter – 10Hz	Two sample t-test	1. Control (N=17) 2. *Cac*^{RNAi} (N=17)	0.027	-0.772	*
	eEPSC jitter – 20Hz	Two sample t-test	1. Control (N=17) 2. *Cac*^{RNAi} (N=18)	0.014	-0.849	*
	eEPSC jitter – 60Hz	Two sample t-test	1. Control (N=17) 2. *Cac*^{RNAi} (N=18)	<0.001	-1.452	***

Figure 5D	Mean firing rate *wt* isopentyl acetate	Two sample t-test	1. Pre GABA block (N=45) 2. Post GABA block (N=45)	<0.001	-0.430	*****
	Mean firing rate *Cac*^{RNAi} isopentyl acetate	Two sample t-test	1. Pre GABA block (N=46) 2. Post GABA block (N=46)	0.065	0.144	n.s
	Mean firing rate *wt* isobutyl acetate	Two sample t-test	1. Pre GABA block (N=43) 2. Post GABA block (N=43)	<0.001	-0.731	*****
	Mean firing rate *Cac*^{RNAi} isobutyl acetate	Two sample t-test	1. Pre GABA block (N=44) 2. Post GABA block (N=44)	0.831	-0.013	n.s
Figure 5E	Mean variance *wt* all odors pooled	Two sample t-test	1. Pre GABA block (N=88) 2. Post GABA block (N=88)	<0.001	-0.583	*****
	Mean variance *Cac*^{RNAi} all odors pooled	Two sample t-test	1. Pre GABA block (N=90) 2. Post GABA block (N=90)	0.154	0.088	n.s
	J-index probability *wt* all odors pooled	Two sample t-test	1. Pre GABA block (N=88) 2. Post GABA block (N=88)	0.893	0.012	n.s
	J-index probability *Cac*^{RNAi} all odors pooled	Two sample t-test	1. Pre GABA block (N=90) 2. Post GABA block (N=90)	0.044	0.216	**
Figure 6B	Learning index	One way ANOVA	1. *Orco-GAL4* (N=40) 2. UAS- *Cac*^{RNAi} (N=37) 3. *Orco-GAL4;* UAS- *Cac*^{RNAi} (N=54)	0.196	0.025	n.s
Figure 6D	Probability of correct choice	One way ANOVA	1. *Orco-GAL4* (N=20) 2. UAS- *Cac*^{RNAi} (N=20) 3. *Orco-GAL4;* UAS- *Cac*^{RNAi} (N=21)	<0.001	0.244	***
Figure S3A	Peak ΔF/F *Cpx*^{RNAi} isopentyl acetate	Two sample t-test	1. Control (N=6) 2. *Cpx*^{RNAi} (N=6)	0.094	-0.985	n.s
	Peak ΔF/F *Cac*^{RNAi} isopentyl acetate	Two sample t-test	1. Control (N=6) 2. *Cac*^{RNAi} (N=8)	<0.001	2.374	***

	Peak ΔF/F *Cpx*^{RNAi} isobutyl acetate	Two sample t-test	1. Control (N=6) 2. *Cpx*^{RNAi} (N=6)	0.106	-0.944	n.s
	Peak ΔF/F *Cac*^{RNAi} isobutyl acetate	Two sample t-test	1. Control (N=6) 2. *Cac*^{RNAi} (N=8)	<0.001	2.956	***
Figure S3B	Mean firing rate *Brp*^{RNAi} linalool	Two sample t-test	1. Control (N=59) 2. *Brp*^{RNAi} (N=49)	0.023	0.445	*
	Mean firing rate *Brp*^{RNAi} isopentyl acetate	Two sample t-test	1. Control (N=72) 2. *Brp*^{RNAi} (N=50)	<0.001	0.667	***
	Mean firing rate *Brp*^{RNAi} 2 heptanone	Two sample t-test	1. Control (N=63) 2. *Brp*^{RNAi} (N=48)	0.088	0.330	n.s
	Mean firing rate *Brp*^{RNAi} ethyl acetate	Two sample t-test	1. Control (N=50) 2. *Brp*^{RNAi} (N=45)	0.837	-0.042	n.s
	Mean firing rate *Brp*^{RNAi} isobutyl acetate	Two sample t-test	1. Control (N=50) 2. *Brp*^{RNAi} (N=50)	0.039	0.418	*
	Mean firing rate *Cpx*^{RNAi} linalool	Two sample t-test	1. Control (N=59) 2. *Cpx*^{RNAi} (N=50)	0.017	0.466	*
	Mean firing rate *Cpx*^{RNAi} isopentyl acetate	Two sample t-test	1. Control (N=72) 2. *Cpx*^{RNAi} i (N=50)	<0.001	0.902	***
	Mean firing rate *Cpx*^{RNAi} 2 heptanone	Two sample t-test	1. Control (N=63) 2. *Cpx*^{RNAi} (N=50)	0.030	0.416	*
	Mean firing rate *Cpx*^{RNAi} ethyl acetate	Two sample t-test	1. Control (N=50) 2. *Cpx*^{RNAi} (N=50)	0.027	0.447	*
	Mean firing rate *Cpx*^{RNAi} isobutyl acetate	Two sample t-test	1. Control (N=50) 2. *Cpx*^{RNAi} (N=50)	<0.001	0.857	***
	Mean firing rate *Cac*^{RNAi} linalool	Two sample t-test	1. Control (N=59) 2. *Cac*^{RNAi} (N=50)	0.015	0.475	*

	Mean firing rate *Cac*^{RNAi} isopentyl acetate	Two sample t-test	1. Control (N=72) 2. *Cac*^{RNAi} (N=50)	<0.001	0.776	***
	Mean firing rate *Cac*^{RNAi} 2 heptanone	Two sample t-test	1. Control (N=63) 2. *Cac*^{RNAi} (N=50)	0.317	0.190	n.s
	Mean firing rate *Cac*^{RNAi} ethyl acetate	Two sample t-test	1. Control (N=50) 2. *Cac*^{RNAi} (N=50)	0.296	0.210	n.s
	Mean firing rate *Cac*^{RNAi} isobutyl acetate	Two sample t-test	1. Control (N=50) 2. *Cac*^{RNAi} (N=50)	0.007	0.545	**
	Mean firing rate *Syn*^{RNAi} linalool	Two sample t-test	1. Control (N=59) 2. *Syn*^{RNAi} (N=50)	0.041	0.396	*
	Mean firing rate *Syn*^{RNAi} isopentyl acetate	Two sample t-test	1. Control (N=72) 2. *Syn*^{RNAi} (N=49)	<0.001	0.828	***
	Mean firing rate *Syn*^{RNAi} 2 heptanone	Two sample t-test	1. Control (N=63) 2. *Syn*^{RNAi} (N=49)	0.111	0.306	n.s
	Mean firing rate *Syn*^{RNAi} ethyl acetate	Two sample t-test	1. Control (N=50) 2. *Syn*^{RNAi} (N=50)	0.028	0.446	*
	Mean firing rate *Syn*^{RNAi} isobutyl acetate	Two sample t-test	1. Control (N=50) 2. *Syn*^{RNAi} (N=50)	0.002	0.619	**
Figure S6	First spike latency *Brp*^{RNAi} mock odor	Two sample t-test	1. Control (N=50) 2. *Brp*^{RNAi} (N=50)	0.877	-0.403	n.s
	First spike jitter *Brp*^{RNAi} mock odor	Two sample t-test	1. Control (N=50) 2. *Brp*^{RNAi} (N=50)	0.913	-0.022	n.s
Figure S7	J-index probability *GluCl*$_{\alpha}^{RNAi}$ all odors pooled	Two sample t-test	1. Control (N=5234) 2. *GluCl*$_{\alpha}^{RNAi}$ (N=3950)	<0.001	-0.230	***